# EVOLUTION OF FISSIONLIKE REACTIONS IN MEDIUM ENERGY HEAVY ION COLLISIONS

By

Jaeyong Yee

### A DISSERTATION

Submitted to
Michigan State University
in partial fulfillment of the requirements
for the Degree of

DOCTOR OF PHILOSOPHY

Department of Physics and Astronomy

1995

# ABSTRACT

# EVOLUTION OF FISSIONLIKE REACTIONS IN MEDIUM ENERGY HEAVY ION COLLISIONS

By

#### Jaeyong Yee

MSU  $4\pi$  Array has been completed with the addition of multiwire proportional counters (MWPC). Bragg curve counters (BCC) have been successfully run in the standalone mode. These detectors combined with other components of the Array enabled the measurement of intermediate mass fragment (IMF:  $3 \le Z \ge 18$ ) as well as light charged particles in coincidence with fissionlike fragments in a  $4\pi$  geometry, over a wide energy range ( $E_{beam}=15-115$  AMeV) for the reaction  $^{40}$ Ar +  $^{232}$ Th. The exclusive folding angle distribution data provide direct evidence that fissionlike processes following incomplete-fusion are still an appreciable exit channel for beam energies as high as 115 AMeV. Three distinct sources of IMF emission are identified by the azimuthal angular correlation function among two fissionlike fragments and an IMF. Respective contributions of the three emission modes to the IMF multiplicity with the beam energy are estimated. Prefission emission gains dominance in this energy range while the evaporation from the fissionlike fragments decreases to the point that its importance becomes comparable to that of simultaneous ternary breakup.

To Grandma

# ACKNOWLEDGEMENTS

Paying respect cannot be done by mimicking the way in which one has not grown. Although I've learned quite a few things in this culture, my sincere thanks and respect can only be expressed in my way. I will call him

#### Gary D. Westfall, The Teacher.

Without his continuous support and encouragement, I'm sure to have left this institute, only to lose my self-confidence. Sometimes I thought his patience would surpass mine toward myself. I am in debt to him.

Professor W. Benenson is thanked for his service during most of my stay as an associate director. He continued to support me even during my not so satisfactory years. Professor J. Kovacs made it possible for me to start all this by accepting me into this department. Professors W. Benenson, P. Danielewicz, J. Kovacs, S. Mahanti, and W. Repko are thanked for their guidance as guidance committee members. Professor W. Repko is acknowledged for his agreement to join the committee in response to my almost unreasonable last minute request.

"Skip" Vander Molen is appreciated for all his yelling and I regret I had to call him up so many times in the middle of the night. D. Swan and J. Yurkon are thanked for their endurance of our detector lab take—over for over a year. They were also most helpful.

The best atmosphere I enjoyed was when W. Ken Wilson and R. Lacey were both around. They initiated my research and made it enjoyable. I wish I had had longer overlap with them. That could have most likely made my life here even easier and happier. E. Gualtieri is one of the unfortunate souls who had no choice but to take the worst of me for so long time. I appreciate all the discussions we had. S. Hannuschke is thanked for his willingness to answer and talk in a very pleasant way.

Lily and Hyunju are two of the most negatively benefited people by all this. I find no means to make it up for them. All I can do is to write here that I love them most.

# Contents

	Abs	tract		i
	Ack	nowle	dgments	iii
1	Intr	oduct	ion	1
	1.1	Physic	es Justification	1
	1.2	Organ	ization of This Thesis	6
2	Exp	erime	${ m nts}$	7
	2.1	Introd	luction	7
		2.1.1	Experimental Design	7
		2.1.2	MSU $4\pi$ Array	7
	2.2	MWP	C	9
		2.2.1	Construction	9
		2.2.2	Signal Processing	11
		2.2.3	Coordinate Determination	11
		2.2.4	Time Analysis	18
		225	Efficiency	99

		2.2.6	Particle Identification
	2.3	Phosw	ich Detectors
		2.3.1	Signals
		2.3.2	Particle Identification
	2.4	Bragg	Curve Counters
		2.4.1	Construction
		2.4.2	EZ Mode
		2.4.3	Ion Chamber Mode
3	Fold	ling A	ngle Analysis 35
U	1010		
	3.1	Introd	uction
		3.1.1	Motivation
		3.1.2	Background
		3.1.3	Present Work
	3.2	Experi	imental Description
	3.3	Definit	tions
		3.3.1	Folding Angle
		3.3.2	Linear Momentum Transfer
	3.4	Analys	sis
		3.4.1	Inclusive Fission Fragment Folding Angle 41
		3.4.2	Out-of-plane Distribution

		3.4.3	IMF Emission Angle and Event Selection	47
		3.4.4	Two Cases of Linear Momentum Transfer	49
		3.4.5	Fissionlike Process Cross Section	49
	3.5	Concl	usion	53
4	IMI	F Emis	ssion in Fissionlike Collisions	<b>5</b> 9
	4.1	Introd	uction	59
		4.1.1	Motivation	59
		4.1.2	Background	60
		4.1.3	Present Work	61
	4.2	Correl	ation Method	61
		4.2.1	High Order Azimuthal Correlation Method	61
		4.2.2	Third Order Azimuthal Correlation Method	61
		4.2.3	Definitions	62
		4.2.4	Interpretation of $\psi_3$	63
	4.3	Event	Selection	65
		4.3.1	Description	65
		4.3.2	Folding Angle and Impact Parameter	67
		4.3.3	Additional Condition	68
	4.4	Analy	sis	70
		111	$C(\psi_{r})$ Distribution	70

5	Con	clusio	n	84
		4.5.3	Summary	80
		4.5.2	Multiplicity of IMF from Each Emission Mechanism	80
		4.5.1	IMF Emission Mechanism	76
	4.5	Concl	usion	76
		4.4.3	Comparison of Data and Simulation	74
		4.4.2	Signature of Neck Emission	71

# List of Figures

1.1	Relative probability of evaporation (E), binary fission (F) and	
	cracking (C) as a function of excitation energy of the $^{131}Xe$ nu-	
	cleus	2
1.2	In-plane angular correlation of fission fragments for the system $^{40}\mathrm{Ar}$	
	+ $^{232}$ Th at 31, 35, 39, and 44 MeV/u	4
1.3	Fission fragment folding angle distributions measured in coinci-	
	dence with Be, C, O, and Ne fragments	5
2.1	(a) A single module that consists of MSU $4\pi$ Array. (b) Side view	
	of MSU $4\pi$ Array	8
2.2	Exploded view of the layers making up an MWPC	10
2.3	(a) Anode signal output from preamp. (b) Cathode signal output	
	from preamp	12
2.4	Cathode signal of one end vs. the other end	13
2.5	Position spectra using a mask that covers a hexagonal type MWPC	
	except for the holes at each corner and lower character 'h' in the	
	center	14

2.6	(a) Cathode coordinate system $(x', y')$ . (b) Module coordinate sys-	
	tem $(x, y, z)$ . (c) The orientation of the unit vectors of module	
	coordinate system in lab. frame. (d) $\mathbf{r} = \mathbf{R} + \mathbf{x} \ldots \ldots$	16
2.7	Angular distribution of MWPC events	17
2.8	(a) Velocity spectra of the particles detected in MWPC. (b) Recoil	
	velocity of the compound nucleus	19
2.9	(a) Ideal case of $t_{RF}$ . (b) Wrapping–around occurred. (c) The RF	
	time signal is clipped on both sides.	20
2.10	Efficiency of MWPC relative to BCC as a function of charge number	
	of nucleus detected is shown in the case of 35 MeV/nucleon $^{40}\mathrm{Ar}$	
	beam	23
2.11	BCC E signal in EZ mode vs. MWPC pulse height.	25
2.12	MWPC pulse height vs. folding angle of the events that either one	
	of the two particles doesn't leave signal in the BCC	26
2.13	Folding angle distribution of $(\Box)$ inclusive data, $(\times)$ IMF-	
	contaminated data, ( $\bigcirc$ ) IMF–suppressed data	27
2.14	Fast output vs. slow output	28
2.15	Particle identification template that assigns charge, mass and en-	
	ergy values to a particle projected onto a certain point	30
2.16	Schematic diagram of BCC	31
2.17	Typical spectra of BCC with the pid gates superimposed	33
2.18	Typical 2-dimensional plot of BCC E vs fast plastic	34

3.1	Distribution of angles that fission axis makes with beam direction.	40
3.2	Inclusive fission fragment folding angle distributions for Ar + Th	
	reactions from 15 to 115 AMeV	42
3.3	Contour plot of $\phi_{ff}$ vs. $\theta_{ff}$ for the reaction of Ar + Th at $E_{beam}$ =	
	15 - 115 AMeV	44
3.4	Fission fragment azimuthal distributions for $Ar + Th$ reaction from	
	15 to 115 AMeV gated on low LMT	45
3.5	Fission fragment azimuthal distributions for $Ar + Th$ reaction from	
	15 to 115 AMeV gated on high LMT	46
3.6	Width of gaussian distributions used to fit the data vs. beam en-	
	ergy	48
3.7	IMF gated folding angles	50
3.8	Average and most probable LMT values in terms of beam momentum. $\frac{1}{2}$	51
3.9	LMT per projectile nucleon	52
3.10	Calculated excitation energy using the hybrid model	54
3.11	Calculated number of prefission emission nucleons	55
3.12	Estimated size of compound nucleus after prefission emission of	
	nucleons	56
3.13	Cross sections for fissionlike processes compared with model pre-	
	diction	57
4.1	Demonstration of $\psi_3$ values with various combination of three az-	
	imuthal separation angles	64

4.2	Azimuthal correlation function $C(\psi_3)$	66
4.3	Contour plot of IMF rapidity in the center of mass frame $(y_{cm})$ and	
	folding angle $(\theta_{ff})$	69
4.4	Azimuthal correlation function $(C(\psi_3))$ vs. $\psi_3$	72
4.5	IMF energy distributions for the reaction $^{40}{\rm Ar}$ + $^{232}{\rm Th}$ at ${\rm E}_{beam}$ =	
	35 A MeV	75
4.6	Azimuthal correlation function distributions for the reaction 40 Ar	
	+ $^{232}$ Th at $E_{beam} = 15$ - $115$ A MeV	77
4.7	Excitation energy of the reaction $^{40}{\rm Ar}$ + $^{232}{\rm Th}$ with varying beam	
	energy	78
4.8	Relative cross sections of three IMF emission modes in fissionlike	
	reaction of $^{40}{\rm Ar}$ + $^{232}{\rm Th}$ at E <sub>beam</sub> 15 – 115 A MeV	81
49	Mean number of IMF associated with each IMF emission mode	82

# Chapter 1

# Introduction

# 1.1 Physics Justification

In medium energy heavy ion collisions ( $E_{beam} \approx 10 \sim 100$  AMeV), when the beam energy is well above the Coulomb barrier, it is known that a hot ( $T \geq 3$  MeV) compound nucleus can be formed [Soye89]. It is of great interest how this hot nucleus decays. Identifying and understanding specific decay modes would provide important insight into nuclear reaction dynamics and ultimately help to characterize the nuclear equation of state. One of the attempts to predict the decay modes and their relative cross section is from the statistical approach. An example is given in Fig. 1.1 that was obtained by microcanonical calculation. It is seen that there are possibly three mechanisms competing, evaporation, binary fission, and cracking.

When a compound nucleus decays through fission, one of the techniques that can best describe the mechanism is angular correlations, namely the folding angle technique. Over the past several years, exhaustive studies of inclusive fragmentfragment folding angle distributions have been performed, and the results from these studies have provided a wealth of insights into linear momentum transfer

Figure 1.1: Relative probability of evaporation (E), binary fission (F) and cracking (C) as a function of excitation energy of the  $^{131}Xe$  nucleus (microcanonical calculation from [Zhen87])

and energy dissipation in heavy ion collisions (see Fig. 1.2). Intuitively, one would expect to get the highest energy dissipation for the most central collisions. At low energies (E  $\leq$  10 AMeV), the reaction is indeed dominated by the fusion process or strongly damped collisions. With increasing beam energy, a quite large number of fast particles having almost the beam velocity can be observed which are very likely emitted during the early stages of the collision. The consequence will be a decrease of the available linear momentum in the entrance channel for fusion. Complete fusion processes will then be strongly reduced, and the so called incomplete fusion or massive transfer process will take place. This process is observed to dominate complete fusion at energies as low as  $E_{beam} \approx 15$  A MeV. It was suggested that fission following the incomplete fusion may not be observed for  $E_{beam} > 40$  AMeV with the folding angle technique [Conj85].

Another aspect to consider is the enhancement of non-equilibrium processes in the early state of the collision. With increasing beam energy, this effect would result in an enhanced number of emitted particles. This enhancement may affect the folding angle distribution, that contains only fissionlike fragments, so that position of the peak located at smaller  $\theta_{ff}$  values would shift. An example of such an effect is shown in Fig. 1.3 .

Now, we have two motivations to investigate more closely the fissionlike reaction. The first is to map out one of the three competing decay modes which is the fissioning of the hot compound nucleus in medium energy heavy ion collisions. The fate of fissionlike reactions with increasing beam energy is not firmly established. Secondly, it becomes more necessary to take IMF emission into account with increasing beam energy when we study fissionlike reaction, because IMFs

Figure 1.2: In-plane angular correlation of fission fragments for the system  $^{40}$ Ar +  $^{232}$ Th at 31, 35, 39, and 44 MeV/u . Curves are drawn to guide the eye. The vertical lines at each energy correspond to  $\theta_{ff}=170^{\circ}$  and 110° (LMT of about 0.8 and 7 GeV/c respectively); the arrows indicate the locations of the full momentum transfer. From [Conj85] .

Figure 1.3: Fission fragment folding angle distributions measured in coincidence with Be, C, O, and Ne fragments detected at  $\theta_{IMF} = -51^{\circ}$  (open points) and  $\theta_{IMF} = +126^{\circ}$  (filled points). Solid lines through points are to guide the eye. Upper solid line represents the inclusive folding angle distribution; its normalization is arbitrary. From [Faty87] .

play a more important role in the decay of hot nucleus with increasing beam energy. The effect of IMF production is not a well addressed subject partly because of the difficulty in the exclusive measurement of fissionlike fragments and IMFs at the same time, for which our detector system is designed.

# 1.2 Organization of This Thesis

This thesis is made of mainly three parts. In Chapter 2, I review the MSU  $4\pi$  Array concerning previously existing components and describe the multiwire proportional counters (MWPC) in detail. The techniques used to extract time and position information are given explicitly. Classification of detected particles along with bragg curve counters (BCC) is demonstrated.

In Chapter 3, I employ a folding angle technique to track the fissionlike reactions in central collisions. In-plane and out-of-plane folding angle distributions are presented. IMF emission along with linear momentum transfer (LMT) is studied. Cross sections for the reaction are obtained and compared with the hybrid model calculations.

In Chapter 4, azimuthal correlation functions are introduced to analyze the fissionlike reaction events. Three distinct modes of IMF emission in central collision fissionlike reaction are identified. Their respective contributions to the relative cross sections with beam energy are estimated and presented in terms of average number of IMF emission from each mode.

In Chapter 5, I summarize the results and give conclusions.

# Chapter 2

# Experiments

# 2.1 Introduction

# 2.1.1 Experimental Design

The experiment was proposed to investigate the disappearance of fusion and the onset of multifragmentation. To probe fusion, folding angle is one of the interesting observables, which requires detecting fissionlike fragments [Conj85]. Study of the onset of multifragmentation requires the detection of IMFs within the same setup. These requirements call for a detection system with wide dynamic range as well as excellent spatial coverage.

# 2.1.2 MSU $4\pi$ Array

The completed MSU  $4\pi$  Array is an ideal detection system for this purpose. It consists of the main ball phoswiches[Cebr90], forward array phoswiches[Wils91], Bragg curve counters(BCC) in ion chamber mode [Li93] and EZ mode[Gual95a], and multiwire proportional counters(MWPC). Individual modules(subarrays) each have all the components (see Fig. 2.1 (a) ) in the concept of logarithmic detection[West85], except for the forward array. A cross sectional view of the

Figure 2.1: (a) A single module that consists of MSU  $4\pi$  Array. (b) Side view of MSU  $4\pi$  Array, that shows the arrangement of each component.

fully assembled array is shown in Fig. 2.1 (b).

# 2.2 MWPC

Low pressure multiwire proportional counters(LP-MWPCs) have been constructed as part of MSU  $4\pi$  Array[West85]. There are two main purposes of this detector subarray. First, it enables us to detect fission fragments with 1° angular resolution. Secondly, due to its fast response time, we now have proper triggering signal to use Bragg Curve Counter (BCC) as standalone EZ detectors. Altogether, the MSU  $4\pi$  Array makes the optimum detection system for the studies that require wide dynamic range of particles as well as spatial acceptance.

#### 2.2.1 Construction

Previously, the MSU  $4\pi$  Array consisted of an inner layer of BCCs in front of a layer of plastic phoswich detectors. In the present configuration, the MWPCs are mounted in front of the BCC, forming the innermost layer of the Array.

The frame of the MWPC is made of 6 layers of G10 fiberglass with kapton foils (0.3 mil) forming front and rear pressure windows. The anode forms the center layer and consists of a plane of 12  $\mu m$  diameter gold–plated tungsten wires spaced 1 mm apart. This layer is between two cathode planes which are made of stretched polypropylene foils. A layer of aluminum is evaporated on the surface of the foil, and is divided into 5 mm wide strips connected by a 1 mm wide strip of resistive (1 k $\Omega$ ) nichrome. (See Fig. 2.2.) The thickness of the layer of evaporated Al, as well as the thickness of the nichrome layer is 1 kÅ. Originally, a thinner nichrome strip was to be used. However problem related to the strength of the

Figure 2.2: Exploded view of the layers making up an MWPC. Charges are collected at the end of each nichrome strip.

10

strip developed. Any minor stress on the foil caused the strip to crack and the resistance to increase significantly. Because of this, the width of the Al strip had to be narrowed to 1 mm in the region where the nichrome strip crosses, so that thicker nichrome strip can be used while maintaining same resistance. Even with these measures taken, the phenomena of rising resistance still remains as a concern, but the problem is greatly lessened.

# 2.2.2 Signal Processing

With an operating condition of 5 torr isobutane gas and +510 V anode bias, we get two types of signals each from the anode and cathode. Anode signals originate from electron avalanche and are intrinsically much faster than cathode signals [Bres79]. We use the anode signal to set up the triggering condition, while the cathode signal is used to give position information. The preamp was designed with two goals in mind. (See Fig. 2.3.) The plateau area in the cathode output corresponds to the charge collected at the end of the nichrome strip. If we plot the amount of collected charge of one end vs. the other end, we get Fig. 2.4. The radiating lines of this fan-like picture represent each aluminum strip, hinting that the position along the line that traverses aluminum strips can be determined. Details are discussed in the next section. An example of the use of the cathode signal to reconstruct the image of a mask in front of an MWPC is presented in Fig. 2.5.

#### 2.2.3 Coordinate Determination

To identify the position of particles in the lab frame where they go into the MWPC, we use 3 different coordinate systems. In addition to these frames, there

Figure 2.3: (a) Anode signal output from preamp. (b) Cathode signal output from preamp. Note that the time interval to be integrated is an order of magnitude bigger than the case of phoswich ( $\sim 100ns$ ).

Figure 2.4: Cathode signal of one end vs. the other end.

Figure 2.5: Position spectra using a mask that covers a hexagonal type MWPC except for the holes at each corner and lower character 'h' in the center.

are 3 distinct types of detector modules, which makes the conversion parameters between the coordinate systems vary.

# ullet Cathode Coordinate System $(\mathbf{x}', \mathbf{y}')$

— This is the natural coordinate system following cathode orientation. Capital A to F mean the charge collected at the end of nichrome wire on the corresponding side. (See Fig. 2.6 (a) ) The coordinates are given as follows;

For hexagon type,

$$x' = \left(\frac{D-A}{D+A}\right) \cdot d_1$$

$$y' = \left(\frac{C-F}{C+F}\right) \cdot d_2.$$
(2.1)

For pentagon type,

$$x' = -\left(\frac{A}{C+A}\right) \cdot (s_1 + s_2) + s_2$$

$$y' = -\left(\frac{E}{B+E}\right) \cdot (s_1 + s_2) + s_2.$$
(2.2)

### • Module Coordinate System (x, y, z)

— x,y axes lie in the same plane defined by x',y'. But the unit vectors are defined as  $\hat{x}=\hat{\Theta}, \hat{y}=\hat{\Phi}, \hat{z}=\hat{R}$ . (See Fig. 2.6 (b),(c) )

$$x = x' \cdot \frac{\sin(\theta + \alpha)}{\sin \theta} - y' \cdot \frac{\sin \alpha}{\sin \theta}$$

$$y = -x' \cdot \frac{\cos(\theta + \alpha)}{\sin \theta} + y' \cdot \left(\frac{\sin \theta + \sin \alpha \cdot \cos(\theta + \alpha)}{\sin \theta \cdot \sin(\theta + \alpha)}\right).$$
(2.3)

Figure 2.6: (a) Cathode coordinate system (x', y'). (b) Module coordinate system (x, y, z). (c) The orientation of the unit vectors of module coordinate system in lab. frame. (d)  $\mathbf{r} = \mathbf{R} + \mathbf{x}$ 

Figure 2.7: Angular distribution of MWPC events.

	hex	pent(6-10)	pent(21-25)
$\theta$	60°	72°	72°
$\alpha$	0	72°	36°

# • Ball Coordinate System $(\mathbf{r}, \theta, \phi; \mathbf{X}, \mathbf{Y}, \mathbf{Z})$

— Same as laboratory frame. It has the origin at target position, and Z is the beam direction. R is pointing the center of each module, that is the origin of the module coordinate system. (See Fig. 2.6 (c),(d))

$$\tan \theta = \left[ \frac{R^2 \sin^2 \Theta + x^2 \cos^2 \Theta + 2Rx \sin \Theta \cdot \cos \Theta + y^2}{R^2 \cos^2 \Theta + x^2 \sin^2 \Theta - 2Rx \sin \Theta \cdot \cos \Theta} \right]^{\frac{1}{2}}$$

$$\tan \phi = \frac{(R \sin \Theta + x \cos \Theta) \cdot \sin \Phi + y \cos \Phi}{(R \sin \Theta + x \cos \Theta) \cdot \cos \Phi - y \sin \Phi}.$$
(2.4)

Data are shown in Fig. 2.7 with identified  $\theta$  and  $\phi$  value of each event. Space that each module occupies is clearly demonstrated divided by the wall area around the module. Target frame shadowing traverses near  $\theta \approx 90^{\circ}$  and one of the rod holding the frame is shown near  $\phi \approx 240^{\circ}$ . Forward modules even show the cathode strips quite well.

# 2.2.4 Time Analysis

In the normal setup of the MSU  $4\pi$  Array, the relative time of flight of each particle with respect to the triggering signal gets recorded for the case of phoswich and MWPC. The time difference between the cyclotron radio frequency (RF) and the triggering signal is also recorded. But, this information was never used to obtain the velocity of a particle directly, partly because we can get the energy values

Figure 2.8: (a) Velocity spectra of the particles detected in MWPC. The line is from Viola's empirical formula. See text for details. (b) Recoil velocity of the compound nucleus. Data are from the reaction  $^{40}\text{Ar} + ^{232}\text{Th}$  at  $\text{E}_{beam} = 35 \text{ AMeV}$ 

Figure 2.9: (a) Ideal case of  $t_{RF}$ . (b) Wrapping-around occurred. (c) The RF time signal is clipped on both sides. The shaded bar on the RF time line is the spread of triggering particle.

from the pulse height in the case of phoswich detectors, which is very difficult for MWPCs. So, we devised a method to obtain the velocity using time information.

It involves three kind of time signals,  $t_{MWPC}$ ,  $t_{RF}$ , and  $t_{phoswich}$ , as well as the energy values of the particles corresponding to  $t_{phoswich}$ . With this reference to the phoswich, the absolute time of flight for the particle recorded in MWPC can be obtained. In Fig. 2.8, we show the results. The validity of this method is checked in Fig. 2.8 (a) with Viola systematics[Viol83], that should match the value at  $\theta_{ff} \approx 180^{\circ}$ . (For  $\theta_{ff}$ , see [Viol89].) Because Viola's empirical formula predicts the kinetic energy of the fission fragment as a function of the charge and mass of the fissioning nucleus in the frame of the fissioning nucleus, the velocity of the fission fragment obtained from peripheral collision is expected to be comparable to that calculated by the formula. Unless a transformation is performed using recoil velocity, the velocity of the fission fragment from a central collision will have slightly higher value than the calculation. Such a trend can be seen in Fig. 2.8 (a) . Recoil velocity data in Fig. 2.8 (b) also shows the agreement with the expected values, since it should go to near zero at  $\theta_{ff} \approx 180^{\circ}$ , which indicates the most peripheral collision.

One thing to give particular attention to is the RF time signal relative to the triggering particle. The typical spread in velocity spectra is  $1 \ cm/ns$ , and the distance between the target and the MWPC is about 15 cm. Thus the typical time spread of the triggering particle is 15 ns, which is same order of magnitude of RF interval. Hence, wrapping—around of  $t_{RF}$  may occur as the beam energy changes. Clipping on both sides in  $t_{RF}$  may occur as the RF interval gets shorter than time spread of triggering particle. In Fig. 2.9, we show those cases from

data. In the case of (b) and (c), the time analysis is inevitably more erratic than in (a).

## 2.2.5 Efficiency

In this experiment, MWPCs are used to detect fissionlike particles. So the detection efficiency is tuned to high Z particles. Although the efficiency relative to the BCC is near 100 % for the particles with  $Z \geq 10$ , the MWPCs still have the capability to detect lighter IMFs with reduced efficiencies. (See Fig. 2.10 .) The response shows little dependency on the beam energy over the range studied.

We were unable to measure the absolute efficiency as a function of Z.

#### 2.2.6 Particle Identification

A measurement of the fission fragment folding angle is meaningful only when the two observed particles, whose velocity vectors make that angle, are both fissionlike fragments. Because we know that the MWPCs we use are quite efficient for IMFs too, we have to identify those events in which either of the signals from MWPCs is generated by an IMF. For the case when a particle leaves a signal in both the MWPC and the backing BCC, we can plot the E signal from the BCC vs. pulse height of the corresponding MWPC as in Fig. 2.11. From the BCC particle identification, we identify the peaked region on the left as IMFs, while the bottom region with small E values are recognized as fissionlike fragments. When a particle is stopped before it reaches BCC, we plot the pulse height vs. folding angle. (See Fig. 2.12.) Unlike the inclusive case in which we don't care whether there is a coincident signal in BCC, the IMFs reveal themselves in the bottom left region. The right region represent valid target fission events.



Combining those two methods, the IMF contamination can be removed in the folding angle plot as seen in Fig. 2.13.

## 2.3 Phoswich Detectors

# 2.3.1 Signals

A phoswich detector produces composite signal of fast and slow components, that depends on the charge and deposited energy of the incoming particles [Wilk52]. Although the charge resolution is not as good as Si detectors, the flexibility of fabrication both in size and shape, and thus possible greater stopping power, make the phoswich the choice of closed packed arrays such as MSU  $4\pi$  Array. By gating the fast and slow components separately and integrating the charge within the gate, we get bands of isotope lines shown in Fig. 2.14.

#### 2.3.2 Particle Identification

The light output as a function of deposited energy from the plastic scintillator is not linear, but rather a complicated function of charge, mass and energy of the incoming particle [Becc76]. The response function for MSU  $4\pi$  Array phoswiches was found to be [Cebr90]

$$(slow\ output) \propto \frac{E^{1.4}}{A^{0.4} \cdot Z^{0.8}}$$

$$(fast\ output) \propto E^{0.5}$$

$$(2.5)$$

where E is the incident energy of the particle with charge Z and mass A. Using an energy-loss program such as DONNA[Meye81], E, Z and A values are mapped out onto a 2-dimensional space as shown in Fig. 2.14. (See Fig. 2.15.) By

Figure 2.11: BCC E signal in EZ mode vs. MWPC pulse height. There are two distinct groups in the left and bottom regions.



Figure 2.13: Folding angle distribution of ( $\square$ ) inclusive data, ( $\times$ ) IMF–contaminated data, ( $\bigcirc$ ) IMF–suppressed data.

Figure 2.14: Fast output vs. slow output.

transforming and overlaying Fig. 2.14 onto Fig. 2.15 and finding the best fit, we assign each particle the charge, mass and incident energy.

# 2.4 Bragg Curve Counters

When a charged particle traverses a volume of gas, it loses energy as it interacts with the gas atoms along the way. Generally, the rate of energy loss increases logarithmically and then increases dramatically just before the particle stops within the gas. After that it falls down sharply. The term Bragg curve refers to this energy loss function, and the peak at the end is called the Bragg peak. The height of the Bragg peak is proportional to the charge of the particle. The total energy loss can be obtained by integrating the Bragg curve [Gruh82].

#### 2.4.1 Construction

The gas chamber is made of G10 fiberglass. On the inside surface, there are field shaping strips connected by 1.55 M $\Omega$  resistors, producing a radial electric field along the path from the entrance kapton window (900  $\mu g/cm^2$ ) to the aluminized surface on the face of the backing phoswich fast plastic which serves as the anode. The entrance window frame does dual duty as the cathode and pressure window. A grounded Frisch grid 1 cm from the anode surface prevents the induced image charge from being collected in the anode. (See Fig. 2.16 ) It was operated with 125 torr  $C_2F_6$  gas at +150 V anode voltage and -500 V of cathode bias.

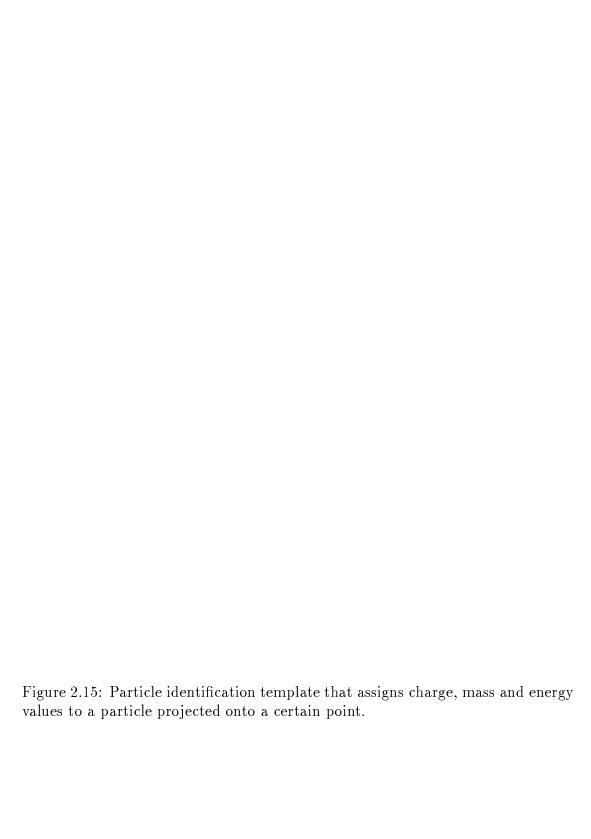


Figure 2.16: Schematic diagram of BCC.

#### 2.4.2 EZ Mode

When a particle stops inside the gas volume, a Bragg peak is produced, and we get both charge and energy information for that particle by measuring the peak height and integrated signal, respectively. Gate lines were drawn by matching the punch—out point with calculations. ELOSS[Zieg85] was used to calculated energy loss and map out energy values. Typical spectra with gate lines superimposed are shown in Fig. 2.17.

#### 2.4.3 Ion Chamber Mode

When a particle punches into the fast plastic and stops there such that it doesn't produce Bragg peak in the gas, we are in much the same situation as in the phoswich. The integrated E signal from BCC vs. fast plastic signal is shown in Fig. 2.18. The response functions are found to be

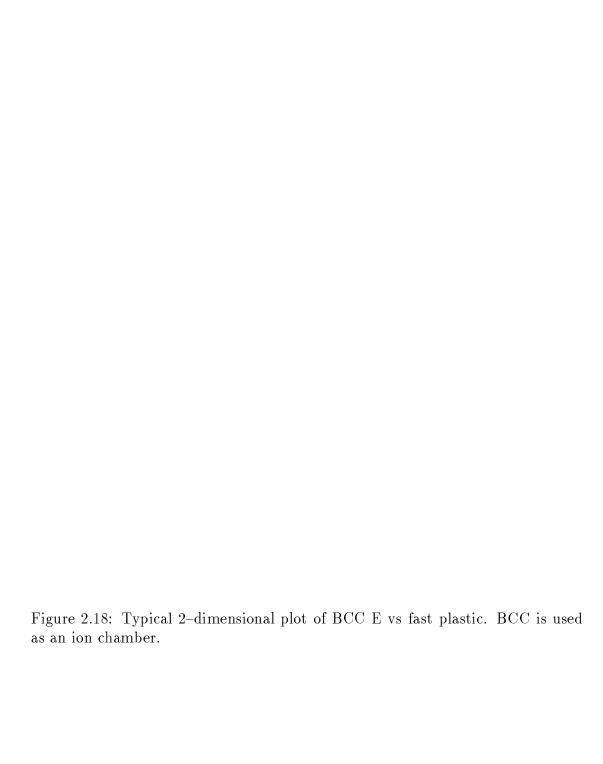
$$(fast\ output) \propto \frac{E^{1.4}}{Z^{0.8} \cdot A^{0.4}}$$

$$(BCC\ E) \propto E^{0.9},$$

$$(2.6)$$

where E is the incident energy. Previous test [Cebr91] has found that the BCC E output is quite linear to incident energy. But, with this setup there was found some non-linearity. The same technique is used as in phoswich to map out charge, mass and energy values.

Figure 2.17: Typical spectra of BCC with the pid gates superimposed.



# Chapter 3

# Folding Angle Analysis

Fission-like fragments and coincident charged particles have been measured in a  $4\pi$  geometry over a wide energy range (15 – 115 AMeV) for the reaction  $^{40}{\rm Ar} + ^{232}{\rm Th}$ . The exclusive folding angle distribution data provide direct evidence that fission-like processes following incomplete-fusion are still an appreciable exit channel for beam energies as high as 115 AMeV.

# 3.1 Introduction

#### 3.1.1 Motivation

Angular correlation studies of fission-like fragments produced via the bombard-ment of highly fissile targets provide important insights into nuclear reaction dynamics. Over the past several years, exhaustive studies of inclusive fragment-fragment folding angle distributions have been performed, and the results from these studies have provided a wealth of insights on linear momentum transfer and energy dissipation in heavy ion collisions[Bege92, Lera84, Poll84, Conj85, Jacq84, Viol89, Tsan84]. However as the beam energy increases, the inclusive fragment-fragment folding angle alone cannot effectively describe the reaction be-

cause intermediate mass fragment (IMF) is expected to play a more important role. Exclusive folding angle data along with wide dynamic range measurement of light charged particles and IMFs is called for. The MSU  $4\pi$  Array is the ideal setup for this kind of measurement.

#### 3.1.2 Background

Fragment-fragment folding angle distributions are typically characterized by two peaks; one at small folding angles (< 180°) and the other at large folding angles (≈ 180°) [Conj85, Jacq84, Viol89, Tsan84, Leeg92, Faty85, Schw94]. The peak at small folding angles is usually attributed to fusion-like reactions or incomplete-fusion resulting in high linear-momentum-transfer (LMT). The other peak, located at large folding angles, is linked to peripheral reactions or target-fission with small LMT. One of the prominent features of folding angle distributions is the rapid decrease of the high linear-momentum-transfer peak with increasing beam energy[Conj85, Jacq84, Viol89, Faty85, Schw94].

In a series of inclusive measurements, Pollacco and Conjeaud observed that the high LMT peak in the folding angle distribution for  $^{40}$ Ar +  $^{232}$ Th is strongly suppressed for beam energies  $E_{beam} \geq 30$  AMeV, and disappears for  $E_{beam} \geq 44$  AMeV[Poll84, Conj85]. Many speculations pertaining to the nature of central heavy ion collisions have been generated by these rather surprising results, and a few exclusive measurements have been performed with the explicit intent of addressing the fate of central Ar + Th collisions for beam energies  $\geq 30$  AMeV[Schw94, Jian89]. Nonetheless the detailed nature of the reaction mechanism remains unclear.

#### 3.1.3 Present Work

In this chapter, we report results from an extensive set of  $^{40}$ Ar +  $^{232}$ Th measurements (E<sub>beam</sub> = 15–115 AMeV) in which we have simultaneously detected light-charged particles, intermediate mass fragments (IMF:  $3 \le Z \le 18$ ), and fission fragments with nearly  $4\pi$  coverage. We observe direct evidence for fission–like reactions in a beam energy range where prior inclusive measurements have pointed to the possible disappearance of such processes. Earlier exclusive measurements for this system have employed setups with significantly less solid angle coverage for the simultaneous detection of fragments and light-charged particles.[Schw94, Jian89].

# 3.2 Experimental Description

The <sup>40</sup>Ar beams [15, 25, 30, 35, 40, 45, 55, 75, and 115 AMeV] used in this experiment were provided by the K1200 cyclotron at the National Superconducting Cyclotron Laboratory (NSCL). The beam intensity was approximately 100 electrical pA and the thickness of the Th target was 1.0 mg/cm². Charged reaction products were detected with the fully configured MSU 4π Array[West85]. The MSU 4π Array consists of a main ball of 170 phoswich detectors (arranged in 20 hexagonal and 10 pentagonal subarrays) covering angles from 23° to 157° and a forward array of 45 phoswich detectors covering angles from 7° to 18°. Thirty multiwire proportional counters (MWPCs) were installed in front of 55 Bragg curve counters (BCCs) which in turn were installed in front of the hexagonal and pentagonal phoswich sub-arrays. The MWPCs and BCCs were operated with 5 torr of isobutane gas and 125 torr of C<sub>2</sub>F<sub>6</sub> gas respectively. In addition to providing Z and E signals for fragments stopped in their active volume, the BCCs

provided  $\Delta E$  signals for charged fragments ( $Z \geq 2$ ) that stopped in the fast plastic scintillator of the main ball. Fission-like fragments were detected in the MWPCs with an angular resolution of  $\approx 1^{\circ}$ . Time signals obtained from these MWPCs allowed the determination of the fragment velocities. The  $4\pi$  Array provided clear Z identification for charges of Z = 1 through 18. Low energy thresholds for the main ball were 17 AMeV, 2 AMeV, and 4 AMeV for fragments of Z=1,3, and 12 respectively. The low energy threshold for the forward array was  $\approx 17$  AMeV. Data were taken with a minimum bias MWPC trigger (one or more charged fragments detected in the MWPCs).

The efficiency of MWPCs relative to BCCs rises from 25% for Z=3 to 100% for  $Z\geq 10$ . Consequently, it was necessary to apply offline gates to separate the fission-like fragments from the IMFs. The fragments which stopped in the BCCs, provided two distinct groups which were identified and assigned to IMFs and fission fragments. Low energy fragments which triggered the MWPCs but left no signal in the BCCs were separated by the pulse height difference.

## 3.3 Definitions

# 3.3.1 Folding Angle

Folding angle  $(\theta_{ff})$  is defined as the angle between two velocity vectors, in this analysis, two fissionlike fragments' velocity vectors. In the Cartesian coordinate system where beam direction is same as z direction, the cosine of the folding angle can be calculated from polar and azimuthal angles of two velocity vectors.

$$\cos\theta_{ff} = \cos\theta \cdot \cos\theta' + \sin\theta \cdot \sin\theta' \cdot \cos(\phi - \phi'). \tag{3.1}$$

 $\theta_{ff}$  can have values between 0° and 180°, inclusively.

The out of plane angle  $(\phi_{ff})$  is defined as the angle between the two planes that are defined by the beam direction and each of the two fissionlike fragment vectors.  $\phi_{ff} = 0^{\circ}$  is taken such that three vectors mentioned above are all in the same plane with beam direction in the middle. When the fissionlike reaction results in this configuration, we call it a perfectly coplanar event.

The fission axis is defined as the line defined by joining the tips of the two fissionlike fragment velocity vectors. Given in Fig. 3.1 is the distribution of the angle that the fission axis makes with the beam direction. Note that the distribution for central collision peaks near  $\theta_{rel}\approx 90^{\circ}$ . That suggests that those events are from symmetric fission.

#### 3.3.2 Linear Momentum Transfer

When a nucleus of charge Z and mass A fissions, it releases, in the mean, a value of kinetic energy  $\langle E_K \rangle$  in the frame of fissioning nucleus. According to Viola's empirical formula [Viol85],

$$\langle E_K \rangle = (0.1189 \pm 0.001) \frac{Z^2}{A^{1/3}} + 7.3(\pm 1.5) MeV.$$
 (3.2)

When the projectile has mass  $M_p$  and energy  $E_p$ , thus momentum  $p_o$ , the average linear momentum transfer  $\langle p \rangle$  is given by the formula that is a function of folding angle  $(\theta_{ff})$  and the angle of one of the fission fragment to the velocity of fissioning nucleus  $(\theta_1)$  [Leeg92].

$$\frac{\langle p \rangle}{p_o} = \left[ \frac{M \langle E_K \rangle}{M_p E_p} \right]^{1/2} \frac{\sin \theta_{ff}}{[2\sin^2(\theta_{ff} - \theta_1) + 2\sin^2\theta_1 - \sin^2\theta_{ff}]^{1/2}}.$$
 (3.3)

Figure 3.1: Distribution of angles that fission axis makes with beam direction. • is for inclusive data.  $\Box$  is for peripheral collision.  $\diamondsuit$  is for central collision.

40

The velocity of fissioning nucleus is roughly the same as the beam direction when compound nucleus is formed, but not so in peripheral collision.

# 3.4 Analysis

#### 3.4.1 Inclusive Fission Fragment Folding Angle

Folding-angle ( $\theta_{ff}$ ) distributions for Ar + Th are shown in Fig. 3.2 for  $E_{beam}=15$ , 25, 30, 35, 45, 55, 75, and 115 AMeV. Events are selected when there are two and only two fission-like fragments (Z > 18) detected in the MWPCs, irrespective of the existence of coincident IMFs or light charged particles. Folding angles were determined [event by event] from the directional unit vectors ( $\mathbf{f}$ ) of these two fission-like fragments:  $\theta_{ff}=\arccos(\mathbf{f_1}\cdot\mathbf{f_2})$ . The angle between the two planes defined by the beam axis and the unit vector of each fragment,  $\phi_{ff}$ , was allowed to vary between  $-90^\circ$  and  $90^\circ$  for these distributions. The double peaked structure which is characteristic of folding angle distributions is clearly visible in Fig. 3.2 for beam energies  $\leq$  45 AMeV. The high and low LMT peaks are located at approximately 110° and 165°, respectively. The energy dependence of these distributions are similar to those previously reported for comparable beam energies[Poll84, Conj85, Schw94]. They corroborate the previous observation that the high LMT peak essentially disappears for  $E_{beam} \approx 50$  AMeV.

# 3.4.2 Out-of-plane Distribution

In Fig. 3.3,  $\phi_{ff}$  vs.  $\theta_{ff}$  is plotted. At low beam energy, two peaks in those contour plots are identified corresponding two peaks in  $\theta_{ff}$  distribution of Fig. 3.2. These contours are symmetric for  $\phi_{ff}=0^{\circ}$ , which means that the fissionlike fragments

Figure 3.2: Inclusive fission fragment folding angle distributions for Ar + Th reactions from 15 to 115 AMeV.

have mostly the same masses. For the high LMT peak, the height decreases while the width stays as beam energy increases, as far as we can identify that peak. We can say quantitatively that the width of  $\phi_{ff}$  increases as the beam energy increases. The low LMT peaks show little change.

To quantify these results, we plot Fig. 3.4 and Fig. 3.5. Note the difference in the scale between figures. The open circles in Fig. 3.4 represent the distributions gated on the low LMT peak,  $\theta_{ff} > 135^{\circ}$ . The solid squares in Fig. 3.5 represent distributions gated on the high LMT peak,  $85^{\circ} \leq \theta_{ff} \leq 135^{\circ}$ . Distributions are shown for several beam energies as indicated in the figure. The widths of the gaussian curves used to fit these distributions are shown in Fig. 3.6 with the same symbolic convention as that of the previous two figures.

A striking feature of this figure is the beam energy dependence of the widths of the  $\phi_{ff}$  distributions for high LMT. In contrast to the widths for the low LMT  $\phi_{ff}$  distributions ( $\approx 30^{\circ}$ ), these widths show a monotonic increase (from 25° to 70°) with increasing beam energy. Because target fission with low LMT is essentially a binary process, one can conclude that the high LMT reaction mechanism becomes increasingly different from a binary one as the beam energy increases. We attribute this trend to a growth in the importance of multi-fragment final states [not necessarily simultaneous multi-fragmentation] with increasing beam energy. It appears that the suppression of the high LMT peak with increasing beam energy (cf. Fig. 3.2) is not only associated with a decrease in the cross section for fission-like processes that follow incomplete-fusion but also with a change in reaction mechanism from an essentially binary one to non-binary one. Therefore, proper selection of multi-fragment final states could lead to selective enhancement

Figure 3.3: Contour plot of  $\phi_{ff}$  vs.  $\theta_{ff}$  for the reaction of Ar + Th at  $E_{beam} = 15 - 115$  AMeV.

Figure 3.4: Fission fragment azimuthal distributions for Ar + Th reaction from 15 to 115 AMeV gated on low LMT. Linear scale.

Figure 3.5: Fission fragment azimuthal distributions for Ar + Th reaction from 15 to 115 AMeV gated on high LMT. Same as Fig. 3.4, but gated on high LMT. Even though it decreases substantially with beam energy, the high LMT distribution maintains its gaussian shape.

of the high LMT peak in the  $\theta_{ff}$  distributions.

#### 3.4.3 IMF Emission Angle and Event Selection

In Fig. 3.7, we compare folding angle distributions for fission-like fragments emitted in multi fragment events. The left column of the figure (Fig. 3.7 (a)-(d)) shows distributions gated on one or more IMFs at forward angles ( $\theta_{lab}$  < 15°). The middle column (Fig. 3.7 (e) - (h) ) shows distributions gated by the detection of one or more IMFs at backward angles ( $\theta_{lab} > 68^{\circ}$ ). The right column (Fig. 3.7 (i) - (l) ) shows distributions gated on the top 10% of the total-transverse-kineticenergy impact parameter filter. The four rows in Fig. 3.7 (from top to bottom) show results for  $E_{beam} = 35, 45, 75, \text{ and } 115 \text{ AMeV}, \text{ respectively.}$  It should be noted here that the cross sections reported in the figure are not corrected for the detection efficiency of the IMFs. In contrast to the double peaked folding angle distributions shown in Fig. 3.2, the distributions shown in Fig. 3.7 are characterized by a single peak which can be linked to either high or low LMT. The distributions gated on forward IMFs show peaks which are clearly associated with low LMT, while the distributions gated on backward IMFs or small impact parameters show the expected peaks for high LMT. As the beam energy increases, the high LMT peak can only be identified when the fission-like fragments are measured along with other particles. This fact is evident when one compares Fig. 3.7 to Fig. 3.2. It is noteworthy that the high LMT peak is well-separated from the low LMT peak even at  $E_{beam} = 115$  AMeV, which provides the direct evidence that the fission-like processes persist up to this beam energy. Moreover, the gating condition requires these events to be non-binary. We conclude that the fission-like process which follows incomplete-fusion is a well-defined exit channel

Figure 3.6: Width of gaussian distributions used to fit the data in Fig. 3.4 and Fig. 3.5 vs. beam energy. The symbols follow the same convention. Straight lines are to guide the eye.

for the entire beam energy range of our measurements and that it changes its characteristics from an essentially binary mechanism [at low energy] to one involving more than two fragments.

#### 3.4.4 Two Cases of Linear Momentum Transfer

Folding angles can be translated into LMT event by event[Leeg92]. We have extracted average LMT values,  $/p_{beam}$ , considering both target-fission as well as fusion-fission. They are estimated to be 86, 70, 62, 54, 41, 32, 23, and 16% for Figs. 1a-1h, respectively. A maximum of 151  $\pm$  11 MeV/c per projectile nucleon is observed for  $E_{beam} \approx 30$  AMeV, which agrees with previous data[Viol89, Tsan84]. The methods used in Fig. 3.7 to identify and enhance the high LMT peak make it possible for us to extract the most probable LMT as well for the entire energy range measured. A maximum of  $172 \pm 11 \text{ MeV/c}$  per projectile nucleon is obtained for  $E_{beam} \approx 30$  AMeV. (See Fig. 3.8 and Fig. 3.9 ). In spite of the difference between the average and most probable LMT values for 30 AMeV, one is still led to the conclusion that there is a limit to the amount of linear momentum that can be transferred from the projectile to the fission-like fragments. This limitation is apparently due to the fact that, with increasing beam energy, a significant fraction of the available momentum is carried away by particles other than fission-like fragments. This is the case identified in the right two columns of Fig. 3.7.

#### 3.4.5 Fissionlike Process Cross Section

In order to gain insight on the evolution of the reaction mechanism, we have performed a simple two stage model calculation [Harp71, Desb87a, Cerr89]. In

Figure 3.7: Fission fragment folding angle distributions for Ar + Th reactions gated on IMFs at forward angles (left column), IMFs at large angles (center column), and central collision impact parameter obtained by the total transverse kinetic energy. Solid lines are gaussian fits to guide the eye.

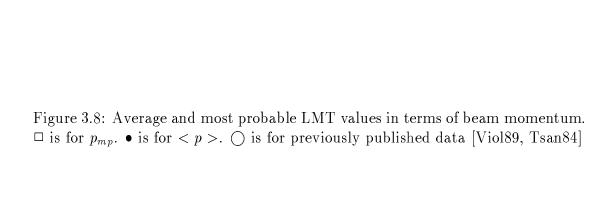


Figure 3.9: LMT per projectile nucleon. Symbols follow the same convention as in Fig. 3.8 .

this model the nucleons of a projectile are trapped inside the potential well of the target, and the resulting system undergoes pre-equilibrium emission of particles and then expands isentropically. Extracted percolation parameters then determine whether the system eventually experiences multifragmentation or fissions. This hybrid model can calculate the excitation energy of the compound nucleus and it is plotted in Fig. 3.10 . It also calculates the number of prefission emission nucleons, which is plotted in Fig. 3.11 . That enables us to estimate the size of compound nucleus after prefission emission of nucleons. (See Fig. 3.12 .)

In Fig. 3.13, the fission-like process cross section from the data is plotted along with the calculation. Both show that there is a substantial decrease in the cross section for fission-like reactions as the beam energy increases, but the model under-predicts the cross section in the high energy range where the non-binary fission takes over the reaction mechanism.

# 3.5 Conclusion

In conclusion, we have performed an extensive set of exclusive folding angle measurements. We see a monotonic decrease (86 % to 16 %) in momentum transfer of the projectile to the fission-like fragments with increasing beam energy. This trend is consistent with the notion that as the beam energy increases more violent collisions occur and large number of particles are ejected each carrying a fraction of the available linear momentum. Apparently the occurrence of pure binary fission seems to be less likely with increasing beam energy and a different reaction mechanism leading to multi body final states takes over. Our exclusive measurement makes it possible to observe fission-like reactions even at  $E_{beam} \approx 115$ 

Figure 3.10: Calculated excitation energy using the hybrid model mentioned in the text.





Figure 3.13: Comparison of the extracted fission-like process cross sections for Ar + Th data (solid circles) with the predictions of the model (open circles). Lines are drawn to guide the eye.

AMeV, and provide direct evidence for the persistence of these reactions albeit in non–binary form over the energy range we studied.

# Chapter 4

# IMF Emission in Fissionlike Collisions

Intermediate mass fragments (IMF:3  $\leq Z \leq 18$ ) in coincidence with fissionlike fragments were measured in the reaction  $^{40}{\rm Ar} + ^{232}{\rm Th}$  at  ${\rm E}_{beam} = 15$  – 115 A MeV. Three distinct sources of IMF emission are identified by the azimuthal angular correlation function among two fissionlike fragments and an IMF. Respective contributions of the three emission modes to the IMF multiplicity with the beam energy are estimated. Prefission emission gains dominance in this energy range while the evaporation from the fissionlike fragments decreases to the point that its importance becomes comparable as that of simultaneous ternary breakup.

# 4.1 Introduction

#### 4.1.1 Motivation

As a transient state between pure binary fission and multifragmentation, fission-like reactions tend to produce one or two IMFs (intermediate mass fragments) [Klot87, Troc89, Hano93]. To study more closely the evolution of the fissionlike reaction with beam energy, it is necessary that the IMF emission mechanism be

examined beyond observing the increase of mean number of IMFs accompanying the fissionlike fragments [Yee95]. By identifying the IMF emission mechanisms, if there are more than one, and estimating the relative contribution of those mechanisms to the IMF production, one can then have a more complete description of the fissionlike reaction mechanism.

#### 4.1.2 Background

At low energy ( $\leq$  10 A MeV), Boger et.al. identified three distinct modes of IMF formation [Boge90]. Those are the two-body breakup of fission or evaporationlike character, IMF ejection from the composite nucleus followed by sequential fission and a simultaneous ternary breakup. Although they mentioned the IMF ejection from fission fragments after their formation and acceleration, the relative cross section was not given for that channel. The fact that the data were only for one energy leaves the question of evolution unanswered.

In a series of experiments geared toward folding angle measurement, the Viola group successfully showed the existence of IMF emission from the neck region of a fissioning nucleus [Faty87, Fiel92], which is similar to alpha–accompanied ternary fission. [Siwe93]. This result also lacks the varying incident energy.

Trockel et.al. used correlation method to demonstrate that their data showed the sequential nature of multifragment emission [Troc87]. They looked at f.f(fission fragment)-f.f., IMF-HR(heavy residue) and IMF-IMF correlations. IMF-f.f.-f.f. correlation would be the natural next step.

#### 4.1.3 Present Work

With MSU  $4\pi$  Array described in Chapter 2, we have the ability to detect fissionlike fragments and IMFs simultaneously with near  $4\pi$  geometric coverage. We ran experiments by bombarding  $^{40}$ Ar to  $^{232}$ Th targets from 15 A MeV to 115 A MeV. The thickness of the target was 1 mg/cm<sup>2</sup>. Beam current was maintained near 100 electrical pA. With this setup, we present the energy dependence of the relative cross section of each IMF emission mechanism, which has not been done in this energy range. To introduce one combining variable of fissionlike fragments and the accompanying IMF, the azimuthal angular correlation method has been adopted.

#### 4.2 Correlation Method

# 4.2.1 High Order Azimuthal Correlation Method

Stemming from interferometry studies, arbitrary order azimuthal angular correlation functions have been used as an alternative way to study multifragment collective flow [Wang91, Jian92]. More recently, the same method has been applied to show the disappearance of collective flow at the balance energy, without referring to the reaction plane [Lace93, Laur94, Buta95].

#### 4.2.2 Third Order Azimuthal Correlation Method

In this analysis, we are interested in the fissionlike reaction where there is one or more IMFs involved. In particular, the relation between individual IMF and two fissionlike fragments is of importance. IMF-IMF correlation is of little concern because such an event is quite rare in this energy range and more importantly because the emission pattern of IMF with respect to the fissionlike fragments is what we are trying to establish. Therefore, the third order azimuthal correlation function involving two fissionlike fragments and one IMF is the suitable choice.

#### 4.2.3 Definitions

Let's consider general case where the event size is M. For  $\omega$ -th order azimuthal correlation, i.e. the azimuthal correlation of  $\omega$  particles out of M fragments, a variable  $\psi_{\omega}$  is introduced, which is the geometric mean of k pairwise azimuthal separations( $\phi_{ij}$ ) between the fragments.

$$\psi_{\omega} = \left(\prod_{ij}^{k} \phi_{ij}\right)^{1/k}, k = \frac{1}{2}\omega(\omega - 1). \tag{4.1}$$

One thing to remember is the possible multiplets of size  $\omega$  for an event in which M fragments are detected, which is  $M!/(M-\omega)!\omega!$ . Appropriate weighting should always be done by this factor.

The correlation function is defined as a ratio of two  $\psi_{\omega}$  distributions.

$$C(\psi_{\omega}) = \frac{Y(\psi_{\omega}; cor)}{Y(\psi_{\omega}; uncor)}.$$
(4.2)

 $Y(\psi_{\omega}; cor)$  is the observed  $\psi_{\omega}$  distribution, while  $Y(\psi_{\omega}; uncor)$  is from the mixed and randomly chosen events.

For the purpose of this analysis, we choose  $\omega = 3$ . Then, the variable  $\psi_3$  can be written in more explicit form.

$$\psi_3 = (\phi_{f_1 - f_2} \cdot \phi_{f_1 - I} \cdot \phi_{f_2 - I})^{1/3}, \tag{4.3}$$

where  $f_i$ , I mean the fissionlike fragment and IMF, respectively. In this kind of selection scheme, the weighting factor should be always the same for any triplet

because two of the triplet elements are fixed with fissionlike fragments and there is only one degree of freedom in terms of choosing IMF. For completeness, let's write down the correlation function for  $\omega = 3$  case.

$$C(\psi_3) = \frac{Y(\psi_3; cor)}{Y(\psi_3; uncor)}. \tag{4.4}$$

### 4.2.4 Interpretation of $\psi_3$

From the definition, the values that  $\psi_3$  can have are between 0° and 120°, inclusively. However, they are not evenly probable. Because we focus our interest on fissionlike events,  $\phi_{f_1-f_2}$  makes a normal distribution around 180° with a width that depends on the incident energy and impact parameter [Yee95]. Therefore, the azimuthal IMF emission angle with respect to either of fissionlike fragment is the determining factor of  $\psi_3$ . In Fig. 4.1, the above two points are demonstrated at the same time. Take the azimuthal angle of one of the fissionlike fragments as 0°. Then, the angle of the other fragment will be  $180^{\circ} - \alpha$ , where  $\alpha$  has been shown to form a normal distribution around  $0^{\circ}$ . Varying  $\phi_I$ , the azimuthal angle of IMF, from  $0^{\circ}$  to  $360^{\circ}$ , the corresponding  $\psi_3$  values are plotted. Regardless of the values of  $\alpha$ , the distributions maintain similar form, demonstrating the  $\phi_I$  as the determining factor. Note that  $\psi_3$  is very sensitive for  $\phi_I$  close to either one of fissionlike fragments' azimuthal angle, while its value changes little for wide range of  $\phi_I$  when the IMF is emitted farther from both of the fissionlike fragments. In fact, if 10° bins are made for  $\psi_3$ ,  $\phi_{f_1-f_2} = \phi_{f_1-I} = \phi_{f_2-I} = 120$ ° and  $\phi_{f_1-f_2}=180^\circ, \phi_{f_1-I}=\phi_{f_2-I}=90^\circ$  make the same bins.

Figure 4.1: Demonstration of  $\psi_3$  values with various combination of three azimuthal separation angles. The distribution maintains similar form from coplanar fissionlike events ( $\alpha=0^{\circ}$ ) to much less probable out-of-plane events ( $\alpha=60^{\circ}$ ). Also, note the sensitive and less sensitive range of  $\psi_3$ .

Let's plot the correlation function  $C(\psi_3)$  for particular cases as a function of  $\psi_3$ . There are three such cases. First is when  $\phi_I$  is independent of the fissionlike fragment emission angle. As expected, in Fig. 4.2 (a), there's no correlation ( $C(\psi_3)$ ) = 1 for all  $\psi_3$ ). The second case is when the IMF is emitted so that its velocity vector forms a cone shape distribution around either one of fissionlike fragment. Fig. 4.2 (b) shows the correlation function in such a case where there is a strong correlation for  $\psi_3 < 80^\circ$  while there is strong anticorrelation for  $\psi_3 > 90^\circ$ . For  $\psi_3 < 30^\circ$ , it is not plotted because such an event is rather an exception and the lack of statistics gives erratic and misleading results. The third case is when IMF is emitted with similar azimuthal separations from the fissionlike fragments. From the reason explained in the previous paragraph,  $C(\psi_3)$  has sharp correlation at the biggest bin of  $\psi_3$ , as shown in Fig. 4.2 (c). All these combined with certain weighting factor, we expect that the azimuthal correlation function from data would look like Fig. 4.2 (d).

### 4.3 Event Selection

### 4.3.1 Description

By examining the IMF emission pattern, we try to explain the evolution of fissionlike reaction in medium energy heavy ion reactions. We analyze events with two fissionlike fragments and one or more IMFs. As described in Chapter 2, we select fissionlike fragments requiring that their charges are greater than that of projectile, in this case 18. MWPC and BCC work cooperatively to accomplish this task. We restrict the range of IMFs to be  $3 \le Z \le 18$ , which is well within the capacity of the detection system. Now that we know that the desired event

Figure 4.2: Azimuthal correlation function  $C(\psi_3)$ . (a), (b) and (c) each represents particular mode of IMF emission while (d) shows the combined correlation function with arbitrary chosen weighting factor.

can be selected properly, we have to think of the way to classify these events by centrality. This is important because the azimuthal correlation function we are considering will not be able to distinguish peripheral collision from sequential ternary breakup. In the former case, the IMF is essentially a projectile particle. In the latter case, the IMF is ejected from composite system prior to scission. We use two observables simultaneously to accomplish this task. Those are the folding angle between the two fissionlike fragments and the rapidity of the IMF in the center of mass frame. In the next two sections, we will describe the details.

#### 4.3.2 Folding Angle and Impact Parameter

In Chapter 3, folding angle is discussed in detail. Simply put, it is an angle between two directional vectors of two fissionlike fragments. This variable is known to be related to linear momentum transfer [Viol89], but it can also be used as a reaction filter [Tsan89]. Comparing the usual impact parameter selection variables such as charged particle multiplicity and midrapidity charge, it can be shown that the events associated with smaller folding angle range are from central collisions, while the events associated with larger folding angle range are from peripheral collisions. This conforms to the fact that the folding angle is inversely proportional to the amount of linear momentum transferred. It is not hard to imagine that in the central collision most of the linear momentum carried by the projectile would be transferred to the composite system, while in peripheral collision it is expected that the projectilelike particle still carries most of the original linear momentum.

#### 4.3.3 Additional Condition

It is shown in Chapter 3 that the IMF polar angle is an efficient tool for centrality cut in the fissionlike reaction. It is well demonstrated that the proper use of the IMF polar angle can reveal the high linear momentum transfer peak buried under the tail of dominant low linear momentum transfer peak, especially as the beam energy increases. To minimize this contamination by peripheral collision, that will surely confuse the relative cross section of IMF emission mode in central collisions, we put an additional condition of IMF rapidity in the center of mass frame in conjunction with folding angle distribution. This variable can be regarded as an extension of IMF polar angle in the laboratory frame. The peripheral collision peak has a tail with comparable intensity to that of the central collision peak (see Fig. 4.3). Efficiency mismatch for IMF detection among the different components of the detection system results in the three distinct peaks near  $\theta_{ff} \approx 100^{\circ}$ . These components should form a single peak. If we use only a 1 dimensional cut on folding, the peripheral collision tail will always be selected also. Considering that the situation worsens with beam energy, it is essential to use a 2 dimensional condition to select events we analyze. As a summary, the detection system is fully capable of collecting data for fissionlike reaction with coincident IMF. We have two centrality variables, folding angle and rapidity of IMF in center of mass frame, that can separate two fission mechanisms that are obviously different but expected to show very similar results in azimuthal correlation functions in certain cases.

Figure 4.3: Contour plot of IMF rapidity in the center of mass frame  $(y_{cm})$  and folding angle  $(\theta_{ff})$ . The peaks near  $\theta_{ff}=100^\circ$  are related to central collision while the strong peak near  $\theta_{ff}=160^\circ$  is from peripheral collision. Note the tail of this strong peak smears into  $\theta_{ff}\approx 100^\circ$  region. Data are from the reaction  $^{40}{\rm Ar}+^{232}{\rm Th}$  at  $E_{beam}=45~{\rm A~MeV}$ .

## 4.4 Analysis

#### 4.4.1 $C(\psi_3)$ Distribution

The azimuthal correlation function technique has been applied to fissionlike reactions with coincident IMF, to exploit the evolution of that reaction mechanism with beam energy. From the correlation function, we deduce the IMF emission pattern associated with fissionlike reactions. Relative cross sections in term of IMF multiplicity are obtained for each emission pattern. In Fig. 4.4, the azimuthal correlation functions  $(C(\psi_3))$  as a function of  $\psi_3$  are presented for central and peripheral collisions. When a projectile just touches the target and the target fissions, we do not expect any azimuthal correlation. Azimuthal separations between IMF, projectilelike particle, and the fissionlike fragments are uncorrelated. On the other hand, the central collisions show a structure in the distribution that is changing its intensity with beam energy. This structure matches the one we predicted in Fig. 4.2 (d). There we considered three distinct IMF emission modes whose combining effect would result in the prediction.

Now that we can say that those three modes may well be the candidates for what happens in the fissionlike reaction, let's consider each one more closely. Earliest in the time line, before the compound nucleus breaks into two comparable size fragments, fissionlike fragments, an IMF could be ejected first. This process may be called a sequential ternary break-up. In this case, the IMF has no information about the breakup angle of fissionlike fragment. Hence, the azimuthal correlation should have flat value of 1, i.e. no correlation (see Fig. 4.2 (a)). During the scission stage, an IMF may be produced simultaneously with two fissionlike fragments. That we will call a simultaneous ternary breakup. Because the IMF is

driven out mainly by the Coulomb force exerted by two fissionlike fragments that move almost back to back in the frame of fissioning nucleus, the resultant Coulomb force directs the IMF along the near perpendicular direction to the fission line. If this happens it is expected that we see a strong correlation for  $\psi_3 \geq 110^{\circ}$ , while for smaller  $\psi_3$ , there would be a strong anticorrelation (see Fig. 4.2 (c) ). After the breakup of compound nucleus, the fully accelerated fissionlike fragment may still emit an IMF. In the frame of fissioning nucleus, the emitted IMF's velocity distribution forms a cone around the fissionlike fragment's velocity vector. Broad strong correlations are expected for  $\psi_3 < 80^{\circ}$ , while for  $\psi_3$  values, with which simultaneously ternary breakup shows strong correlation, there is strong anticorrelation. Lacking any of those emission mode, it is not possible to reproduce the data with any combination of weighting factor. Simultaneous ternary breakup and emission from fully accelerated fissionlike fragment are obviously necessary from Fig. 4.4. Not so obvious is that sequential ternary fission is also necessary to make the distribution's intensity comparable to data. To summarize, we proposed three distinct modes of IMF emission in fissionlike reaction. The proposition is plausible because data and the prediction using only those emission modes show a qualitative match.

### 4.4.2 Signature of Neck Emission

It has been known that at low energy ( $E_{beam} < 10 \text{A MeV}$ ), there exists ternary fission involving  $\alpha$  emission [Sowi86, Vand73]. A recent study investigated such an emission for the same system as ours ( $^{40}\text{Ar} + ^{232}\text{Th}$ ) but at lower energy ( $E_{beam} \approx 9 \text{ A MeV}$ ) [Siwe93]. They found that it is necessary to introduce near scission emission of  $\alpha$  particles in addition to the prefission emission and the emission

Figure 4.4: Azimuthal correlation function  $(C(\psi_3))$  vs.  $\psi_3$ . Open squares  $(\Box)$  are for central collisions, and closed circles  $(\bullet)$  are for peripheral collisions.  $C(\psi_3)=1$  means no correlation.  $\psi_3<30^\circ$  region is not plotted because of the lack of statistics. Such a case does not have different meaning from  $C(\psi_3)\simeq 50^\circ$  so that dropping that region does not affect the argument. Data are from the reaction  $^{40}{\rm Ar}+^{232}{\rm Th}$  at  $E_{beam}=15-115$  A MeV.

from fully accelerated fragments to explain the energy distribution of detected  $\alpha$  particles. The component in the  $\alpha$  energy distribution from near scission emission is located between those of the other two emission modes. Prefission  $\alpha$ 's always have bigger energy values than near scission emission  $\alpha$ 's. They also observed that the near scission emission is from necklike structure so that the  $\alpha$  particles are emitted preferentially in the direction perpendicular to the fission axis. Those are two of the prominent signatures of near scission emission  $\alpha$ 's from necklike structures.

Near scission emission (NSE) of IMFs from necklike structures is much less frequently observed than that of  $\alpha$ . It has been reported such an event was observed for the system formed in high linear momentum transfer reaction [Fiel92]. High linear momentum transfer is one of the two centrality cut criteria we used and it loosely selects central collision events. They identified neck emission using the energy and emission angle criteria mentioned above. They observed unusually low energy components near the emitting direction perpendicular to fission axis.

Lower energies and preferred perpendicular emission angle to the fission axis are now established as the signatures of IMF emission from necklike structure at near scission stage. With Fig. 4.5 we check if we observe such a signature. Recall that the smaller  $\psi_3$  values get, the closer the IMF emission angle is to either of fissionlike fragment velocity vectors. As  $\psi_3$  approaches its maximum value 120°, IMF emission angle is nearly perpendicular to the fission axis. The former cases are Fig. 4.5 (a) and (b), and the latter are Fig. 4.5 (c) and (d). Notice the emerging shoulder in lower energy range in IMF energy distribution as  $\psi_3$  gets larger. We attribute that shoulder to the signature of neck emission. The fact

that it emerges only when  $\psi_3$  values become large and that it emerges on the smaller energy value side satisfies the conditions previously established. Another thing to note is that perpendicular directional emission alone cannot ensure the neck emission. The high energy component does not change intensity very much with  $\psi_3$ , hinting that sequential ternary fission is dominant in this beam energy. Because such emission should be isotropic, it will also populate the direction near perpendicular to the fission axis with stronger intensity than that of neck emission. But as shown in Fig. 4.2 (a) and (c), the behavior in correlation function will be very different between the two cases. Here, we verified that we indeed observed near scission emission of IMF from necklike structures.

#### 4.4.3 Comparison of Data and Simulation

We now established three components that make the azimuthal correlation function distribution in central collision. With these, we tried to simulate the experimental data. The simulation is semi-empirical in that the experimental distribution in space for the fissionlike fragments is used to sample the events. Sequential ternary breakup is simple. The IMF emission angle is taken isotropically around the fissioning nucleus. In the case of simultaneous ternary breakup, the IMF emission direction is randomly chosen from a normal distribution around the line that is equally distant from the fissionlike fragment vectors in the fissioning nucleus frame. When an IMF is emitted from a fully accelerated fission fragment, its velocity vector, viewed from fissioning nucleus frame, forms a cone shape around fissionlike fragment velocity vector. We pick the direction randomly from the normal distribution around the fissionlike fragment velocity. Now we have two free parameters. Those are the widths of the two normal distributions mentioned

Figure 4.5: IMF energy distributions for the reaction  $^{40}{\rm Ar} + ^{232}{\rm Th}$  at  ${\rm E}_{beam} = 35$  A MeV for different ranges in  $\psi_3$  values.  $\psi_3 = 30^{\circ} \sim 60^{\circ}, 60^{\circ} \sim 80^{\circ}, 80^{\circ} \sim 100^{\circ},$  and  $100^{\circ} \sim 120^{\circ}$ , for (a), (b), (c), and (d), respectively.

above. There are two more parameters. Because we need relative contribution from each of three emission modes, when two of the modes in the sampling are set, the other one is determined. By varying these parameters, we find the best fit. The result is presented in Fig. 4.6. This simple simulation is quite successful in reproducing experimental result throughout the energy range observed. The result is not very sensitive to the first two parameters determining the width of normal distribution. What governs the shape of the correlation function is the relative frequency of sampling. Two things can be said. The three IMF emission modes can explain what's happening in the fissionlike reaction when it produces coincident IMF. Over the energy range we present, there is no need to introduce another major emission mode. What's changing is relative probability of each emission mode, not the emission mechanism itself.

#### 4.5 Conclusion

#### 4.5.1 IMF Emission Mechanism

We showed that the three IMF emission modes could explain the data throughout the energy range studied. The only change is how each mode is weighted. This may be understood considering the change in excitation energy. We established the absence of saturation in energy deposition [Gual95b].

The excitation energy increases with beam energy without saturation in this beam energy range (see Fig. 4.7). A qualitative deduction can be followed for the relative cross section of each IMF emission mode. As the excitation energy increases, a hotter compound nucleus would form. Such a nucleus is more likely to emit small fragments at the earlier stage than less excited nucleus. Consequently,

Figure 4.6: Azimuthal correlation function distributions for the reaction  $^{40}$ Ar +  $^{232}$ Th at  $E_{beam} = 15 - 115$  A MeV. Only central collisions are considered. Open squares ( $\square$ ) are experimental data. Closed circles ( $\bullet$ ) are from simulation.

Figure 4.7: Excitation energy of the reaction  $^{40}\mathrm{Ar} + ^{232}\mathrm{Th}$  with varying beam energy. For the model calculation, see Refs. [Cerr89, Desb87a, Gual95b, Harp71].

it is expected that the sequential ternary breakup mode would gain its importance as beam energy increases.

On the contrary, emission from fully accelerated fissionlike fragment would be less probable as the excitation energy gets larger. More excitation energy would be carried away before the breakup occurs, and the size and excitation energy available to the fissioning nucleus would be smaller and less. Hence we expect smaller and less excited fissionlike fragment as the excitation energy gets larger. Smaller sized fissionlike fragments have been observed with increasing beam energy for the same system [Conj85]. Near scission emission from necklike structure would also gain its share. Because of the smaller size of the fissionlike fragments, there would be less chance that the neck emitting IMF be reabsorbed before it is driven away by the resultant Coulomb force of two fissionlike fragments.

In Fig. 4.8 the relative cross sections of those three IMF emission modes are presented in percentage. At the lowest energy, sequential ternary breakup and emission from fully accelerated fissionlike fragments occur at about the same rate, consuming all the cross section. Simultaneous ternary fission exists, but during only a few percent of time it actually happens. As beam energy increases, and also as the excitation increases at the same time sequential ternary breakup gradually takes up around 80 % of the cross section and flattens out at about  $E_{beam} = 45$  A MeV. Meanwhile, the emission mode from fully accelerated fissionlike fragments decreases down to around 10 % at  $E_{beam} \approx 45$  A MeV and continues to do so although much less rapidly. Simultaneous ternary breakup cross section increases its share through the beam energy range we studied. At  $E_{beam} \approx 75$  A MeV, this mode becomes almost as probable as the emission of IMF from fully accelerated

fissionlike fragments and surpasses that mode at  $E_{beam} \approx 115$  A MeV reducing nearly 10 % of the cross section. Those observation agrees well with qualitative predictions deduced from excitation energy data.

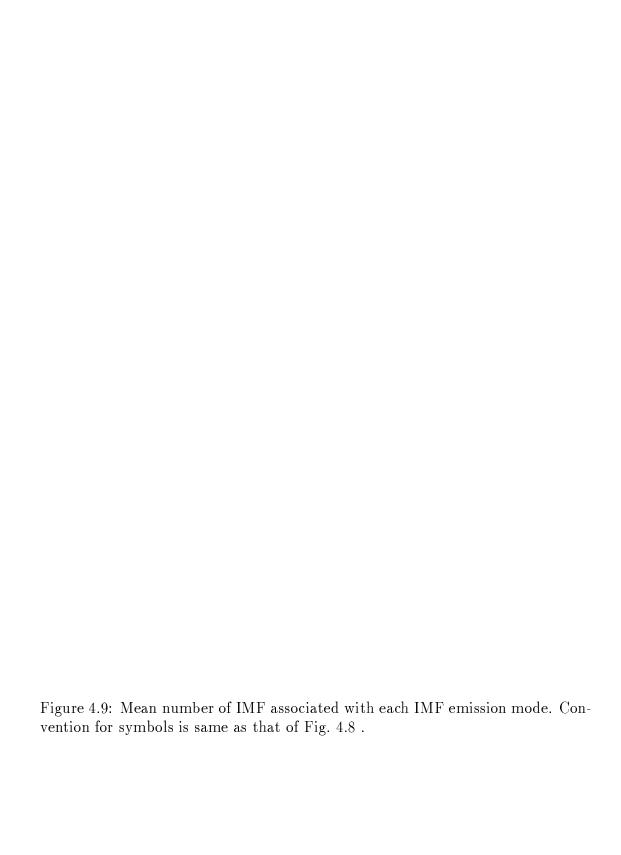
#### 4.5.2 Multiplicity of IMF from Each Emission Mechanism

To give more physical meaning to the ratio in Fig. 4.8, we plot the mean number of IMFs as a function of incident energy (see Fig. 4.9). Note the projectilelike particles in peripheral collision do not count here. Because the overall mean number of IMFs changes smoothly, the distribution does not show a significant difference from that of Fig. 4.8. However, we expect this distribution to be different from that of  $\alpha$  particle emission mode. Siwek-Wilezynska et. al. [Siwe93] reported a result for  $\alpha$  particle emission in the same reaction as ours at  $E_{beam} \approx 9$  AMeV. Their beam energy is just one step below our lowest energy. They observed the prefission emission as a dominant mode while we expect that to be less important than emission from a fully accelerated fragment (postfission emission in their terms). Near scission emission is most rare in their case also, but the relative cross section is much larger in the case of  $\alpha$  in which it is about one—third that of postfission emission. In the case of IMFs, near scission emission at that beam energy is not certain to be observed. We were unable to find any reference to compare to the IMF emission mode.

### 4.5.3 Summary

We applied the azimuthal correlation method to study the evolution of the IMF emission mechanism in fissionlike reactions. The variable  $\psi_3$  is defined such that the azimuthal separation of IMF emission from either of fissionlike fragment is

Figure 4.8: Relative cross sections of three IMF emission modes in fissionlike reaction of  $^{40}\mathrm{Ar} + ^{232}\mathrm{Th}$  at  $\mathrm{E}_{beam}$  15 – 115 A MeV.  $\square$  is for sequential ternary breakup.  $\bullet$  is for the emission from fully accelerated fissionlike fragment.  $\diamondsuit$  is for simultaneous ternary breakup that near scission emission from necklike structure.



represented by that variable. To avoid the confusion caused by projectile fragments, we used a folding angle technique along with the rapidity of accompanying IMF. This effectively removes the contamination from the peripheral collisions. We try to explain the azimuthal correlation function distribution by introducing three components of IMF emission mode. Sequential ternary breakup that occurs before scission is one. Next in the time line is simultaneous ternary breakup that occurs during scission. After the scission, when the fissionlike fragment are fully accelerated, there is another mode of IMF emission from those fragments. Using only these three mechanism, we successfully reproduce the data by simulation. As beam energy increases, the first and third mechanism exchange their dominance so that sequential ternary breakup prevails at higher energy range. Simultaneously ternary breakup starts out being insignificant but increases constantly so that at the highest energy range it wins over the emission mode from fully accelerated fissionlike fragments, although still makes up only around 10 % of the relative cross section. Arguments employing excitation energy can predict this result qualitatively.

# Chapter 5

# Conclusion

As a transient decay mode of hot nuclei between evaporation and multifragmentation, fission evolves in itself from pure binary mechanism to one that involves IMF emission. To study this evolution of fissionlike reaction, one has to make exclusive measurements over a wide dynamic range from light charged particle to fission fragments. We completed the MSU  $4\pi$  Array with the addition of multiwire proportional counter (MWPC) as a fission fragment detector. In addition to that, by successfully operating Bragg curve counters (BCC) in standalone E-Z mode, we were able to lower the energy threshold of IMF measurement, at the same time effectively detecting IMFs with near beam charge.

With this setup, we first tried to establish the existence of a fissionlike reaction mechanism to the extent where such a mechanism had been believed negligible. A folding angle technique is employed while we show that the coincident IMF emission angle can serve as a reaction filter. We see a monotonic decrease in linear momentum transfer (LMT) with beam energy. From there, we confirm the notion that more smaller particles are ejected, with increasing beam energy, each carrying away a fraction of the linear momentum available to fissionlike fragments.

Consequently, the occurrence of pure binary fission decreases in its frequency. Still, we provide direct evidence for the persistence of fissionlike reactions even at  $E_{beam} \approx 115$  AMeV, albeit in non-binary form.

Now that we have shown the existence of multi body fissionlike reactions, we tried to look more closely into the source of IMF emission. By doing so, we expect to understand in more detail the mechanism that leads into the observed final states. The azimuthal correlation method turned out to be an excellent way to do this because it deals with two fissionlike fragments and one coincident IMF altogether and makes the relation into one variable. We identify two IMF emission modes that have a more direct relation with fissionlike reaction and a third mode. The former two are sequential ternary breakup and simultaneous breakup of compound nucleus and the latter is the emission from fully accelerated fissionlike fragment. We were able to reproduce the data with these three emission mechanism over the energy range we studied. Sequential ternary breakup gains its dominance with beam energy, while the emission from the fully accelerated fissionlike fragment loses its importance down to the point that the continuously increasing simultaneous ternary breakup mode surpasses that mode at the highest energy we have. Excitation energy values over the energy range can qualitatively explain this change in relative cross section of each IMF emission mode.

As a conclusion, we show the direct evidence of fissionlike reaction throughout the energy range we studied. Binary breakup where the accompanying IMF, if any, is emitted after scission decreases while ternary breakup where the accompanying IMF is emitted on or before scission becomes prevailing. Sequential ternary breakup in which the IMF is emitted before scission happens around 80 % of the

time, while simultaneous ternary breakup happens about 10 % of the time, at the highest energy we measured. This result contrasts with the case at the lowest energy we measured, in which only about 50 % of the cross section is from sequential ternary breakup, and the simultaneous ternary breakup is negligible.

# **Bibliography**

- [Awes81] T. C. Awes, G. Poggi, C. K. Gelbke, B. B. Back, B. G. Glagola, H. Breuer, and V. E. Viola, Phys. Rev. C 24, 89 (1981).
- [Back80] B. B. Back, K. L. Wolf, A. C. Mignerey, C. K. Gelbke, T. C. Awes,H. Breuer, V. E. Viola, and P Dyer, Phys. Rev. C 22, 1927 (1980).
- [Becc76] F. D. Becchetti, C. E. Thorn, and M. J. Levine, Nucl. Inst. and Meth. **138**, 93 (1976)
- [Bege92] M. Begemann-Blaich, Th. Blaich, M. M. Fowler, J. B. Wilhelmy, H.
  C. Britt, D. J. Fields, L. F. Hansen, R. G. Lanier, D. J. Massoletti,
  M. N. Namboodiri, Y. D. Chan, A. Dacal, A. Harmon, J. Pouliot, R.
  G. Stokstad, S. Kaufman, F. Videbaek, and Z. Fraenkel, Phys. Rev.
  C 45, 677 (1992)
- [Biza86] G. Bizard, R. Brou, H. Doubre, A. Drouet, F. Guilbault, F. Hanappe,
  J. M. Harrasse, J. L. Laville, C. Lebrun, A. Oubahadou, J. P. Party,
  J. Peter, G. Ployart, J. C. Steckmeyer, and B. Tamain, Nucl. Phys.
  A456, 173 (1986).

- [Blai92] Th. Blaich, M. Begemann-Blaich, M. M. Fowler, J. B. Wilhelmy,
  H. C. Britt, D. J. Fields, L. F. Hansen, M. N. Namboodiri, T. C.
  Sangster, and Z. Fraenkel, Phys. Rev. C 45, 689 (1992).
- [Bloc92] J. Blocki, R. Planeta J. Brzychczyk, and K. Grotowski, Z. Phys. A 341, 307 (1992).
- [Boge90] J. Boger, S. Kox, G. Auger, J. M. Alexander, A. Narayanan, M. A. McMahan, D. J. Moses, M. Kaplan, and G. P. Gilfoyle, Phys. Rev. C 41, R801 (1990).
- [Bres79] A. Breskin, R. Chechik, and N. Zwang, Nucl. Inst. and Meth. **165**, 125 (1979)
- [Buta95] A. Buta, J. C. Angélique, G. Auger, G. Bizard, R. Brou, C. Cabot,
  Y. Cassagnou, E. Creme, D. Cussol, Y. El Marsri, Ph. Eudes, M.
  Gonin, K. Hagel, Z. Y. He, A. Kerambrun, C. Lebrun, R. Legrain,
  J. P. Patry, A. Péghaire, J. Peter, R. Popescu, R. Regimbart, E.
  Rosato, F. Saint-Laurent, J. C. Steckmeyer, B. Tamain, E. Vient,
  and R. Wada, Nucl. Phys. A584, 397 (1995).
- [Carj86] N. Cârjan, A. J. Sierk, and J. R. Nix, Nucl. Phys. **A452**, 381 (1986).
- [Casi89] G. Cassini, P. R. Maurenzig, A. Olmi, and A. A. Stefanini, Nucl. Inst. and Meth. A277, 445 (1989)
- [Cebr90] D. A. Cebra, Michigan State University, Ph.D. thesis (1990)
- [Cebr91] D. A. Cebra, S. Howden, J. Karn, D. Kataria, M. Maier, A. Nadasen,C. A. Ogilvie, N. Stone, D. Swan, A. Vander Molen, W. K. Wilson,

- J. S. Winfield, J. Yurkon, and G. D. Westfall, Nucl. Inst. and Meth, A300, 518 (1991)
- [Cerr88] C. Cerruti, J. Desbois, R. Boisgard, C. Ngô, J. Natowicz, and J. Nemeth, Nucl. Phys. A476, 74 (1988).
- [Cerr89] C. Cerruti, R. Boisgard, C. Ngô and J. Desbois, Nucl. Phys. A492,322 (1989)
- [Chbi91] A. Chbihi, L. G. Sobotka, Z. Majka, D. W. Stracener, V. Abenante, T. M. Semkow, N. G. Nicolis, D. C. Hensley, J. R. Beene, and M. L. Halbert, Phys. Rev. C 43, 652 (1991).
- [Conj85] M. Conjeaud, S. Harar, M. Mostefai, E. C. Pollacco, C. Volant, Y. Cassagnou, R. Dayras, R. Legrain, H. Oeschler, and F. Saint Laurent, Phys. Lett. 159B, 244 (1985)
- [Desb87a] J. Desbois, R. Boisgard, C. Ngô, and J. Nemeth, Z. Phys. A328, 101
  (1987)
- [Desb87b] J. Desbois, Nucl. Phys. **A466**, 724 (1987).
- [Duek82a] E. Duek, L. Kowalski, M. Rajagopalan, J. M. Alexander, T. W. Debiak, D. Logan, M. Kaplan, M. S. Zisman, and Y. LeBeyec, Z. Phys. A 307, 237 (1982).
- [Duek82b] E. Duek, L. Kowalski, M. Rajagopalan, J. M. Alexander, D. Logan,M. S. Zisman, and M. Kaplan, Z. Phys. A 307, 721 (1982).

- [Faty85] M. Fatyga, K. Kwiatkowski, V. E. Viola, C. B. Chitwood, D. J. Fields, C. K. Gelbke, W. G. Lynch, J. Pochodzalla, M. B. Tsang, and M. Blann, Phys. Rev. Lett. 55, 1376 (1985)
- [Faty85a] M. Fatyga, K. Kwiatkowski, H. J. Kwiatkowski, L. W. Woo, and V.E. ViolaPhys. Rev. C 32, 1496 (1985).
- [Faty87] M. Fatyga, K. Kwiatkowski, V. E. Viola, W. G. Wilson, M. B. Tsang, J. Pochodzalla, W. G. Lynch, C. K. Gelbke, D. J. Fields, C. B. Chitwood, Z. Chen, and Nayak, Phys. Rev. Lett. 58, 2527 (1987).
- [Fiel89] D. J. Fields, T. C. Sangster, M. L. Webb, B. A. Remington, H. C. Britt, L. F. Hansen, R. G. Lanier, D. Massoletti, M. N. Namboodiri, G. L. Struble, M. Begemann-Blaich, T. Blaich, M. M. Fowler, J. B. Wilhelmy, S. Kaufman, F. Videbaek, Y. D. Chan, A. Dacal, A. Harmon, J. Pouliot, R. G. Stokstad, and Z. Fraenkel Nucl. Phys. A495, 209c (1989).
- [Fiel92] D. J. Fields, K. Kwiatkowski, K. B. Morley, E. Renshaw, J. L. Wile,
  S. J. Yennello, V. E. Viola, and R. G. Korteling, Phys. Rev. Lett.
  69, 3713 (1992).
- [Gali82] J. Galin, H. Oeschler, S. Song, B. Borderie, M. F. Rivet, I. Forest, R. Bimbot, D. Gardès, B. Gatty, H. Guillemot, M. Lefort, B. Tamain, and X. Tarrago, Phys. Rev. Lett. 48, 1787 (1982).
- [Gali85] Joël Galin, Nucl. Phys. **A447**, 519c (1985).
- [Gali94] J. Galin and U. Jahnke, J. Phys. G: Nucl. Part. Phys. 20 1105 (1994)

- [Glas83] P. Glässel, D. v. Harrash, H. J. Specht, and L. Grodzins, Z. Phys. A310, 189 (1983).
- [Gruh82] C. R. Gruhnm, M. Binimi, R. Loveman, W. Pang, M. Roach, D. K. Scott, A. Shotter, T. J. Symons, J. Wouters, M. Zisman, R. Devries, Y. C. Peng, and W. Sondheim, Nucl. Inst. and Meth., 196, 33 (1982)
- [Gual95a] E. E. Gualtieri, Michigan State University, Ph.D. thesis (1995)
- [Gual95b] E. E. Gualtieri, J. Yee, D. Craig, S. Hannuschke, R. A. Lacey, T. Li, W. J. Llope, A. Nadasen, E. Norbeck, R. Pak, N. Stone, A. M. Vander Molen, J. S. Winfield, G. D. Westfall, and S. J. Yennello, Phys. Lett. 357B, 7 (1995).
- [Hano93] K. Hanold, L. G. Moretto, G. F. Peaslee, G. J. Wozdiak, D. R. Bowman, M. F. Mohar, and D. J. Morrissey, Phys. Rev. C 48, 723 (1993).
- [Hara87] S. Harar, Nucl. Phys. **A471**, 205c (1987).
- [Harp71] G. D. Harp, and J. M. Miller, Phys. Rev. C 3, 1847 (1971)
- [Ikez94] H. Ikezoe, Y. Nagame, I. Nishinaka, Y. Tomita, K. Ideno, and T. Ohtsuki, Phys. Rev. C 49, 968 (1994).
- [Jacq84] D. Jacquet, E. Duek, J. M. Alexander, B. Borderie, Phys. Rev. Lett.
   53, 2226 (1984)
- [Jacq85] D. Jacquet, J. Galin, B. Borderie, D. Gardes, D. Guerreau, M. Lefort, F. Monnet, M. F. Rivet, X. Tarrago, E. Duek, and J. M. Alexander, Phys. Rev. C 32, 1594 (1985).

- [Jacq85a] D. Jacquet, J. Galin, M. F. Rivet, R. Bimbot, B. Borderie, D. Gardès, B. Gatty, D. Guerreau, I. Kowalski, M. Lefort, and X. Tarrago, Nucl. Phys. A445, 140 (1985).
- [Jacq90] D. Jacquet, G. F. Peaslee, J. M. Alexander, B. Borderie, E. Duek,
   J. Galin, D. Gardes, C. Grégoire, D. Guerreau, H. Fuchs, M. Lefort,
   M. F. Rivet, and X. Tarrago, Nucl. Phys. A511, 195 (1990).
- [Jian89] D. X. Jiang, H. Doubre, J. Galin, D. Guerreau, E. Piasecki, J. Pouthas, A. Sokolov, B. Cramer, G. Ingold, U. Jahnke, E. Schwinn, J. L. Charvet, J. Frehaut, B. Lott, C. Magnago, M. Morjean, Y. Patin, Y. Pranal, J. L. Uzureau, B. Gatty, and D. Jacquet, Nucl. Phys. A503, 560 (1989)
- [Jian92] J. Jiang, D. Beavis, S. Y. Chu, G. Fai, S. Y. Fung, Y. S. Jiang, D. Keane, Q. J. Liu, Y. M. Liu, Y. Shao, M. Vient, and S. Wang, Phys. Rev. Lett. 68, 2739 (1992).
- [Klot87] G. Klotz-Engmann, H. Oeschler, E. Kankeleit, Y. Cassagnou, M. Conjeaud, R. Dayras, S. Harar, M. Mostefai, R. Legrain, E. C. Pollacco, and C. Volant, Phys. Lett. 187B, 245 (1987).
- [Lace93] R. A. Lacey, A. Elmaani, J. Lauret, T. Li, W. Bauer, D. Craig, M. Cronqvist, E. E. Gualtieri, S. Hannuschke, T. Reposeur, A. M. Vander Molen, G. D. Westfall, W. K. Wilson, J. S. Winfield, J. Yee, S. J. Yennello, A. Nadasen, R. S. Tickle, and E. Norbeck, Phys. Rev. Lett. 70, 1224 (1993).

- [Laur82] F. Saint Laurent, M. Conjeaud, D. Dayras, S, Harar, H. Oeschler, and C. Volant, Phys. Lett. 110B, 372 (1982).
- [Laur94] J. Lauret, R. A. Lacey, A. Elmaani, A. Tsepetis, A. Moores, G. D. Westfall, D. Craig, E. E. Gualtieri S. Hannuschke, T. Li, W. J. Llope, R. Pak, N. Stone, A. M. Vander Molen, J. Yee, A. Nadasen, R. S. Tickle, and E. Norbeck, Phys. Lett. 339B, 22 (1994).
- [Leco95] J. F. Lecolley, L. Stuttgé, M. Aboufirassi, B. Bilwes, R. Bougault, R. Brou, F. Cosmo, J. Colin, D. Durand, J. Galin, A. Genoux-Lubain, D. Guerreau, D. Horn, D. Jacquet, J. L. Laville, F. Lefebvres, C. Le Brun, O. Lopez, M. Louvel, M. Mahi, C. Meslin, M. Morjean, A. Péghaire, G. Rudolf, F. Scheibling, J. C. Steckmeyer, B. Tamain, S. Tomasevic, Phys. Lett. 354B, 202 (1995).
- [Leeg92] H. K. W. Leegte, A. L. Boonstra, J. D. Hinnefeld, E. E. Koldenhof, R. H. Siemssen, K. Siwek-Wilczyńska, Z. Sosin, J. Wilczyński, and H. W. Wilschut, Phys. Rev. C 46, 991 (1992)
- [Lera84] S. Leray, G. Nebbia, C. Gregoire, G. La Rana, P. Lhenoret, C. Mazur,
  C. Ngô, M. Ribrag, E. Tomasi, S. Chiodelli, J. L. Charvet, and C.
  Lebrun, Nucl. Phys. A425, 345 (1984)
- [Li93] T. Li, Michigan State University, Ph.D. thesis (1993)
- [Lope89] J. A. López and J. Randrup, Nucl. Phys. A491, 477 (1989).
- [Meye81] W. G Meyer, unpublished

- [Morr85] D. J. Morrissey, G. J. Wozniak, L. G. Sobotka, R. J. McDonald, A.
   J. Pacheco, and L. G. Morreto Nucl. Phys. A442, 578 (1985).
- [Nebb92] C. Nebbia, J. A. Ruiz, D. Fabris, G. Viesti, R. H. Burch, F. Gramegna, G. Prete, A. Giorni, A. Lleres, J. B. Viano, B. Chambon, B. Cheynis, A. Demeyer, D. Drain, D. Guinet, X. C. Hu, M. Gonin, K. Hagel, J. B. Notowita, R. Wada, and P. L. Gonthier, Phys. Rev. C 45, 317 (1992).
- [Nife85] H. Nifenecker, J. Blachot, J. Crançon, A. Gizon, and A. Lleres, Nucl. Phys. A447, 533c (1985).
- [Ngo88] C. Ngô, Nucl. Phys. A488, 233c (1988).
- [Ngo89] C. Ngô, H. Ngô, S. Leray, and M. E. Spina, Nucl. Phys. A499, 148(1989).
- [Paga94] A. Pagano, S. Aiello, E. De Filippo, G. Lanzanó, S. Lo. Nigro, C.Milone, and M. C. Mermaz, Phys. Rev. C 50, 891 (1994).
- [Poll84] E. C. Pollacco, M. Conjeaud, S. Harar, C. Volant, Y. Cassagnou, R. Dayras, R. Legrain, M. S. Nguyen, H. Oeschler, and F. Saint-Laurent, Phys. Lett. 146B, 29 (1984)
- [Poll88] E. C. Pollacco, Y. Cassagnou, M. Conjeaud, R. Dayras, S. Harar,
   R. Legrain, J. E. Sauvestre, and C. Volant, Nucl. Phys. A488, 319c
   (1988).
- [Poll93] E. C. Pollacco, C. Volant, Y. Cassagnou, M. Conjeaud, R. Dayras, S.Harar, R. Legrain, and J.-E. Sauvestre, Z. Phys. A 346, 63 (1993).

- [Rana83] G. La Rana, C. Nebbia, E. Tomasi, C. Ngô, X. S. Chen, S. Leray, P. Lhenoret, R. Lucas, C. Mazur, M. Ribrag, C. Cerruti, S. Chiodelli, A. Demeyer, D. Guinet, J.L. Charvet, M. Morjean, A. Peghaire, Y. Pranal, L. Sinopoli, and J. Uzureau, Nucl. Phys. A407, 233 (1983).
- [Schr89] W. U. Schröder and J. R. Huizenga, Nucl. Phys. **A502**, 473c (1989).
- [Schw89] E. Schwinn, B. Cramer, G. Ingold, U. Jahnke, D. Hilscher, M. Lehmann, H. Rossner, Nucl. Phys. A502, 551c (1989).
- [Schw94] E. Schwinn, U. Jahnke, J. L. Charvet, B. Cramer, H. Doubre, J. Fréhaut, J. Galin, B. Gatty, D. Guerreau, G. Ingold, D. Jacquet, D. X. Jiang, B. Lott, M. Morjean, C. Magnago, Y. Patin, J. Pouthas, E. Piasecki, and A. Sokolow, Nucl. Phys. A568, 169 (1994).
- [Sikk62] T. Sikkeland, E. L. Haines, and V. E. Viola, Phys. Rev. 125, 1350 (1962).
- [Siwe93] K. Siwek-Wilczynska, J. Wilczynski, H. K. W. Leegte, R. H. Siemssen, H. W. Wilschut, K. Grotowski, A. Panasiewicz, Z. Sosin, and A. Wieloch Phys. Rev. C 48, 228 (1993).
- [Soko93] A. Sokolov, D. Guerreau, J. L. Charvet, B. Cramer, H. Doubre, J. Fréhaut, J. Galin, B. Gatty, G. Ingold, D. Jacquet, U. Jahnke, D. X. Jiang, B. Lott, C. Magnago, M. Morjean, Y. Patin, E. Piasecki, J. Pouthas, and E. Schwinn, Nucl. Phys. A562, 273 (1993).
- [Sowi86] M. Sowiński, M. Lewitowicz, R. Kupczak, A. Jankowski, N. K. Skobelev, and S. Chojnacki, Z. Phys. A 324, 87 (1986).

- [Soye89] Nuclear Matter and Heavy Ion Collisions, edited by M. Soyeur, H. Flocard, B. Tamain, and M. Porneuf, NATO ASI series, Series B: Physucs Vol. 205, Plenum, 1989
- [Troc87] R. Trockel, U. Lynen, J. Pochozalla, W. Trautmann, N. Brummund,
  E. Eckert, R. Glasow, K. D. Hildenbrand, W. F. J. Müller, D. Pelte,
  H. J. Rabe, H. Sann, R. Santo, H. Stelzer, and R. Wada, Phys. Rev.
  Lett. 59, 2844 (1987).
- [Troc89] R. Trockel, K. D. Hildenbrand, U. Lynen, W. F. J. Müller, H. J. Rabe, H. Sann, H. Stelzer, W. Trautmann, R. Wada, E. Eckert, P. Kreutz, A. Kühmichel, J. Pochozalla, and D. Pelte, Phys. Rev. C 39, 729 (1989).
- [Tsan83] M. B. Tsang, D. Ardouin, C. K. Gelbke, W. G. Lynch, Z. R. Xu, B. B. Back, R. Betts, S. Saini, P. A. Baisden, and M. A. McMahan, Phys. Rev. C 28, 747 (1983).
- [Tsan84] M. B. Tsang, D. R. Klesch, C. B. Chitwood, D. J. Fields, C. K. Gelbke, W. G. Lynch, H. Utsunomiya, K. Kwiatkowski, V. E. Viola Jr., and M. Fatyga, Phys. Lett. 134B, 169, (1984)
- [Tsan89] M. B. Tsang, Y. D. Kim, N. Carlin, Z. Chen, R. Fox, C. K. Gelbke, W. G. Gong, W. G. Lynch, T. Murakami, T. K. Nayak, R. M. Ronningen, H. M. Xu, F. Zhu, L. Sobotka, D. Stracener, D. G. Stracener, Z. Majka, V. Abenante, and H. Griffin, Phys. Lett. 220B, 492 (1989).

- [Tsan90] M. B. Tsang, Y. D. Kim, N. Carlin, Z. Chen, C. K. Gelbke, W. G. Gong, W. G. Lynch, T. Murakami, T. K. Nayak, R. M. Ronningen, H. M. Xu, F. Zhu, L. Sobotka, D. Stracener, D. G. Stracener, Z. Majka, and V. Abenante, Phys. Rev. C 42, R15 (1990).
- [Utle94] D. Utley, R. Wada, K. Hagel, J. Li, X. Bin, M. Gui, Y. Lou, R. Tezkratt, J. B. Natowitz, and M. Gonin Phys. Rev. C 49, R1737 (1994).
- [Vand73] R. Vandenbosch and J. R. Huizenga, Nuclear Fission, Academic Press, 1973
- [Verg93] P. Vergani, E. Gadioli, E. Vaciago, E. Fabrici, E. Gadioli Erba, M. Galmarini, G. Ciavola, and C. Marchetta, Phys. Rev. C 48, 1815 (1993).
- [Viol82] V. E. Viola, B. B. Back, K. L. Wolf, T. C. Awes, C. K. Gelbke, H. Breuer, Phys. Rev. C 26, 178 (1982).
- [Viol83] V. E. Viola, K. Kiwatkowski and M. Walker, Phys. Rev. C 31, 1550 (1983)
- [Viol85] V. E. Viola, K. Kiwatkowski and M. Walker, Phys. Rev. C 31, 1550 (1985).
- [Viol87] V. E. Viola, Nucl. Phys. **A471**, 53c (1987).
- [Viol89] V. E. Viola, Nucl. Phys. **A502**, 531c (1989)

- [Vola87] C. Volant, M. Conjeaud, S. Harar, M. Mostefai, E. C. Pollacco, Y. Cassagnou, R. Dayras, R. Legrain, G. Klotz-Engmann, and H. Oeschler, Phys. Lett. 195B, 22 (1987).
- [Wang91] S. Wang, Y. Z. Jiang, Y. M. Liu, D. Keane, D. Beavis, S. Y. Chu, S. Y. Fung, M. Vient, C. Hartnack, and H. Stöcker, Phys. Rev. C 44, 1091 (1991).
- [West85] G. D. Westfall, J. E. Yurkon, J. Van Der Plicht, Z. M. Koenig, B. V. Jacak, R. Fox, G. M. Crawley, M. R. Maier, and B. E. Hasselquist, Nucl. Inst. and Meth. A238, 347 (1985)
- [Wilk52] D. H. Wilkinson, Rev. Sci. Inst. 23, 414 (1952)
- [Wils91] W. K. Wilson, Michigan State University, Ph.D. thesis (1991)
- [Yee95] J. Yee, E. E. Gualtieri, D. Craig, S. Hannuschke, T. Li, W. J. Llope, R. Pak, N. Stone, A. M. Vander Molen, G. D. Westfall, J. S. Winfield, S. J. Yennello, R. A. Lacey, A. Nadasen, E. Norbeck, Phys. Lett. 356B, 191 (1995).
- [Zhan94] H. Zhang, Z. Liu, J. Xu, X. Qian, Y. Qiao, C. Lin and K. Xu, Phys. Rev. C 49, 926 (1994).
- [Zhen87] Y. Zheng, H. Massmann, S. Xu, D. H. E. Gross, X. Zhang, Z. Lu, and B. Sa, Phys. Lett. 194B, 183 (1987).
- [Zieg85] J. F. Ziegler, et. al., "The stopping power and range of ions in solids",Pergamon Press (1985)

[Zing93] R. A. Zingarelli, L. C. Dennis, M. A. Tiede, R. C. Kline, K. W. Kemper, and S. V. Mitchell, Phys. Rev. C 48, 651 (1993).